High-fidelity dendritic sodium spike generation in human layer 2/3 neocortical pyramidal neurons

Helen M. Gooch[1], Tobias Bluett[1], Madhusoothanan B. Perumal[1], Hong D. Vo[1], Lee N. Fletcher[1], Jason Papacostas[2], Rosalind L. Jeffree[3], Martin Wood[2], Michael J. Colditz[3], Jason McMillen[2], Tony Tsahtsarlis[2], Damian Amato[2], Robert Campbell[2], Lisa Gillinder[1,2], and Stephen R. Williams[1,*]

[1] Queensland Brain Institute, The University of Queensland; Brisbane, Queensland, Australia.

[2] Mater Centre for Neurosciences, Mater Hospital; Brisbane, Queensland, Australia.

[3] Royal Brisbane and Women's Hospital; Brisbane, Queensland, Australia.

***Corresponding author**. Email: srw@uq.edu.au

Abstract

Dendritic computations signaled into neuronal output by the initiation and propagation of regenerative dendritic spikes are a feature of the electrical operation of rodent neocortical pyramidal neurons, that have a central role in neocortical circuit function. However, it remains poorly explored whether these mechanisms are operational in the human neocortex. To directly compare the dendritic computational properties of the most numerous class of pyramidal neuron in the human and rat neocortex we made simultaneous electrical recordings from the soma and apical dendrites of layer 2/3 pyramidal neurons maintained in acute brain slices of analogous cortical areas under identical experimental conditions. In both species correlated dendritic excitatory input led to the initiation of sodium channel-mediated dendritic spikes, which had stereotyped biophysical properties. Dendritic sodium spikes in human and rat layer 2/3 pyramidal neurons could be generated across a similar wide input range, exhibited a similar frequency range of activation, and forward propagated with high fidelity to drive neuronal output. Our findings therefore reveal that the dendritic computational properties of human layer 2/3 pyramidal neurons are phylogenetically conserved.

Introduction

The human neocortical mantle is a highly evolved structure [1], made up of hundreds of functionally and anatomically defined areas [2]. Although the neuronal classes which form local neocortical circuits are largely preserved across mammalian species [3,4], the dendritic tree of excitatory pyramidal neurons of the human neocortex are morphologically elaborated and harbour a greater number of dendritic spines than those of homologous neurons in rodents and other primates [3,5,6]. In the rodent neocortex, the dendrites of pyramidal neurons are electrically active and powerfully influence neuronal output by the generation of regenerative dendritic spikes [7-11], which are engaged during *in vivo* circuit computations [12-21]. Elaboration of the dendritic tree of human neocortical pyramidal neurons may therefore be one of the factors underlying the enhanced computational capacity of the human neocortex.

Pioneering dendritic recordings of human layer 2/3 (L2/3) and layer 5 (L5) neocortical pyramidal neurons have revealed that human dendrites are electrically excitable and capable of initiating regenerative dendritic spikes [22-24]. Surprisingly, however, the properties of dendritic electrical excitability and the computational operations executed in the dendritic trees of human neocortical pyramidal neurons have been reported to be divergent from those of rodents [22-24]. Specifically, simultaneous recordings from the apical dendrites of human layer 5 (HL5) pyramidal neurons have shown that dendritic spikes are highly compartmentalized within the apical dendritic tree, and have a minimal impact on action potential (AP) generation [24], in contrast to the well-characterized powerful forward propagation of apical dendritic spikes in rodent L5B pyramidal neurons that drive AP burst firing [7,8,11,24-26]. Recent work has, however, suggested that this disparity may be influenced by the experimental sampling of distinct classes of L5 pyramidal neurons between species, with significant dendritic calcium electrogenesis found in molecularly identified subcortically projecting L5 pyramidal neurons of both taxa [27].

Notably, it has recently been reported that the dendritic integrative operations of human L2/3 (HL2/3) pyramidal neurons are mechanistically and functionally divergent from those of the rodent, with direct recordings demonstrating the initiation and forward propagation of calcium channel-mediated apical dendritic spikes [22], a dendritic spike generation mechanism not apparent in rodent L2/3 pyramidal neurons [10,14,28,29]. This

fundamental species-specific difference in active dendritic integration has been suggested to transform the dendritic computations implemented by HL2/3 pyramidal neurons, allowing the execution of anti-coincidence computations, as calcium-channel mediated dendritic spikes were found to be activated only within a narrow range of dendritic excitatory input [22]. As such anti-coincidence computations are distinct from the correlative computations executed throughout the dendritic trees of rodent pyramidal neurons [8,28,30-33] that have prominent roles in neuronal circuit operations in the rodent neocortex [12-15,17,18,21,34] and other circuits [35-37], we sought to compare the dendritic integrative properties of L2/3 pyramidal neurons of the human temporal cortex with those of an analogous neocortical area of the rodent under identical experimental conditions. We find that dendritic excitatory input in human and rat L2/3 pyramidal neurons is locally integrated at dendritic sites, but surprisingly in both species dendritic spikes are mediated by dendritic sodium channels. Dendritic sodium spikes could be generated across a wide range of correlated excitatory input, at high repetition frequencies, and powerfully forward propagated to drive neuronal output in both human and rat L2/3 pyramidal neurons to implement stereotyped computations. Thus, our findings reveal that the computational capacity of HL2/3 pyramidal neurons is not transformed by a divergence of integrative mechanisms, but is enhanced by the implementation of a phylogenetically conserved dendritic spiking mechanism in the larger and more complex dendritic trees of HL2/3 pyramidal neurons.

Results

Morphological and electrical architecture of human and rat L2/3 pyramidal neurons

To examine the electrophysiological and morphological properties of pyramidal neurons of the human and rodent neocortex we prepared acute brain slices of the human temporal cortex, obtained from patients who had undergone neurosurgery for the alleviation of refractory epilepsy, or the removal of sub-cortical brain tumours (Supplementary Tables 1 and 2), and an analogous neocortical area of the rat, the temporal associative neocortex [24]. High-resolution reconstruction of the dendritic morphology of biocytin-filled pyramidal neurons distributed throughout layers 2 and 3 of the human and rodent temporal cortex revealed that the apical and basal dendritic trees of HL2/3 pyramidal neurons were significantly larger and more complex than those of rat L2/3 (RL2/3) pyramidal neurons (distance from neocortical surface: HL2/3= 824 ± 45 μm, range= 449 - 1203 μm, n= 20 reconstructed neurons; RL2/3= 343 ± 19.5 μm, range= 212 - 540 μm, n= 20 reconstructed neurons; Fig. 1a,b, Supplementary Fig. 1). Quantitative analysis showed that the number of primary dendrites, the path lengths, and the number of branch points in the basal and apical dendritic trees of HL2/3 pyramidal neurons were significantly greater, longer, and more complex than RL2/3 pyramidal neurons (primary dendrites: HL2/3= 7.4 ± 0.3, RL2/3= 5.9 ± 0.3, Mann Whitney U= 81.5, P= 0.0006; apical path length= HL2/3= 780.4 ± 14.8 μm, RL2/3= 358.1 ± 7.9 μm, t-test, df= 467, P< 0.0001; basal path length: HL2/3= 211.0 ± 3.1 μm, RL2/3= 133.6 ± 2.2 μm, Mann Whitney U= 123035, P< 0.0001; apical branch points: HL2/3= 39.7 ± 2.9, RL2/3= 17.3 ± 1.1, Mann Whitney U= 7.5, P< 0.0001; basal branch points: HL2/3= 36.8 ± 2.4, RL2/3= 24.2 ± 1.3, t-test, df= 38 , P< 0.0001; Fig. 1c-h). Furthermore, the calibre of basal and apical dendrites as they emerged from the somata of HL2/3 pyramidal neurons were greater in diameter than in RL2/3 pyramidal neurons; however, the calibre of the main apical dendrite of HL2/3 pyramidal neurons tapered and was similar in diameter to that of RL2/3 pyramidal neurons at the first major bifurcation (Supplementary Fig. 1).

How do such differences in the size and complexity of the dendritic tree influence the electrical structure of pyramidal neurons of each species? To experimentally test this, we made simultaneous somatic and apical dendritic whole-cell recordings from human

and rat L2/3 pyramidal neurons, and examined the electrical attenuation of simulated excitatory postsynaptic potentials (sEPSPs) as they spread from the somatic or dendritic site of generation through the dendritic tree. Simulated EPSPs were generated by the injection of uniform current waveforms, and exhibited indistinguishable kinetics when generated at and recorded from the soma of human and rat L2/3 pyramidal neurons (driving current: amplitude= 200 pA; τ_{rise}= 0.5 ms; τ_{decay}= 5 ms; somatic 10-90 % rise-time: human= 3.47 ± 0.10 ms, n= 48, rat= 3.62 ± 0.08 ms, n= 31, t-test, *P*= 0.23; somatic half-width: human= 21.82 ± 0.32 ms, rat= 20.57 ± 0.61 ms, t-test, *P*= 0.08; Fig. 2). To determine the electrical architecture, we first quantified the attenuation of the amplitude of dendritic sEPSPs as they spread from apical dendritic site of generation to the soma (Fig. 2a). In both species the somatic amplitude of dendritically generated sEPSPs progressively decreased as sEPSPs were generated from increasingly remote apical dendritic sites (dendro-somatic voltage transfer, Fig. 2b). To our surprise when we plotted the degree of dendro-somatic voltage transfer for recordings made from human and rat L2/3 pyramidal neurons against recording distance from the soma the data fell on a similar curve, which could be fit with an exponential function (length constant= 154 μm, n= 48 HL2/3, n= 31 RL2/3; Fig. 2b). Similarly, when we recorded the somato-dendritic voltage transfer of somatically generated sEPSPs (Fig. 2a,c), or calculated the somatic impact of dendritic sEPSPs (Fig. 2a,d) we found distance-dependent relationship which described similar curves in human and rat L2/3 pyramidal neurons (length constants, 641 μm, 642 μm, respectively). These data suggest that the attenuation of sEPSPs in the apical dendritic tree of human and rat L2/3 pyramidal neurons is governed by the physical distance between somatic and dendritic recording sites, and does not exhibit species-specific characteristics. Consistent with this interpretation, analysis of dendritic recordings made at comparable physical distances from the soma of human and rat L2/3 pyramidal neurons revealed that the degree of voltage attenuation, and the somatic impact of dendritic sEPSPs, were not statistically different (human distance range= 80 - 192 μm, n= 21; rat distance range= 80 - 191 μm, n= 25; soma-dendrite transfer: human= 0.81 ± 0.02, rat= 0.79 ± 0.02, t-test, *P*= 0.39; dendrite-soma transfer= human= 0.56 ± 0.03, rat= 0.46 ± 0.05, t-test, *P*= 0.07; somatic impact: human= 0.80 ± 0.02, rat= 0.78 ± 0.02, t-test, *P*= 0.31). Furthermore, the pattern of somato-dendritic attenuation of voltage responses generated by the steps of negative

current injected at somatic sites in rat and human L2/3 pyramidal neurons described a similar relationship (amplitude= -100pA; length constant= 708 μm; Fig. 2j). To explore if this relationship also held for the electrical filtering of the time-course of synaptic events, we analysed the somatic rise-time of dendritically generated sEPSPs, finding a distance-dependent slowing of the somatic rise-time as sEPSPs were generated from increasingly remote dendritic sites in human and rat L2/3 pyramidal neurons (Supplementary Fig. 2). Analysis revealed that this relationship also had a similar structure between species, and consequently the somatic rise-times of sEPSPs generated from comparable dendritic sites were similar between human and rat L2/3 pyramidal neurons (human distance range= 80 - 192 μm, n= 21; rat distance range= 80 - 191 μm, n= 25, human 10-90 % rise time= 4.60 ± 0.11, rat 10-90 % rise time= 4.72 ± 0.09; t-test, *P*= 0.42; Supplementary Fig. 2).

As the attenuation and filtering of synaptic potentials in neurons is principally determined by the passive properties of the somatic and dendritic membrane [38], such distance-dependent relationships would be expected to diverge if biophysical properties such as specific membrane capacitance were distinct between species. Notably, recent work has shown that the specific membrane capacitance of HL2/3 pyramidal neurons is significantly lower than that of RL2/3 pyramidal neurons [39], and divergent from previous measurements [40], a biophysical adaptation predicted to enhance the somatic impact of dendritic EPSPs and accelerate their time-course [39]. As our direct dendritic recordings do not support such a species-specific adaptation, we next determined the specific membrane capacitance of human and rat neurons by examining the charging responses of nucleated patches excised from identified L2/3 pyramidal neurons [40] (Fig. 2e). In each nucleated patch examined, charging responses evoked by brief, small amplitude voltage pulses (7 ms, -5 mV) were well described by a single exponential function, with time constants of 21.0 ± 1.8 ms in HL2/3, and 24.7 ± 1.6 ms in RL2/3 pyramidal neurons (Fig. 2e). Following measurement of the geometry of nucleated patches we calculated near identical values of specific membrane capacitance in human and rat L2/3 pyramidal neurons (human: 0.98 ± 0.03 $\mu F/cm^2$; rat: 0.97 ± 0.04 $\mu F/cm^2$; t-test, df= 29, *P*= 0.91; Fig. 2f). Together, therefore, these data reveal that the attenuation of single sEPSPs in the dendritic tree of human and rat L2/3 pyramidal neurons obey a similar distance-dependent rule, governed by invariant biophysical constants. Given this, our findings indicate that the electrical

architecture of the apical dendritic tree of L2/3 pyramidal neurons is not conserved between species, with the physically larger HL2/3 pyramidal neurons also exhibiting greater electrical distribution.

We next investigated if such relationships diverged when the complexity of simulated synaptic waveforms was increased. When trains of five closely spaced sEPSPs were generated at dendritic sites, we found that the distance-dependent decrement of the somatic impact of dendritic sEPSP trains fell on a similar curve in human and rat L2/3 pyramidal neurons (sEPSP trains generated at 50 Hz; driving current: amplitude= 200 pA; τ_{rise}= 0.5 ms; τ_{decay}= 5 ms; length constant= 679 μm; Fig. 2g,h). Notably, however, when the effects of dendritic cable filtering on the somatic amplitude of sEPSP trains was compensated for by scaling the amplitude of the first sEPSP of trains [41], a normalization of the somatic impact of sEPSP trains generated at dendritic and somatic sites was apparent in HL2/3 (slope= -0.14 per 1 mm), but not RL2/3 pyramidal neurons (slope= 0.6 per 1 mm; Fig. 2l), a phenomenon only previously observed in other neuronal classes in the rodent neocortex and hippocampus [41,42]. Consistent with this, in HL2/3 pyramidal neurons the somatic half-width of single dendritic sEPSPs generated widely across the apical dendritic tree was not determined by the site of generation in the dendritic tree, but was similar to sEPSPs generated at the soma (slope: 0.15 per 1 mm; Supplementary Fig. 3). In other neuronal classes such time-course normalization is mediated by the sculpting of EPSPs by the influence of hyperpolarization-activated cyclic nucleotide-modulated (HCN) channels [41,42]. Consistent with the involvement of HCN channels in this behaviour we observed that HL2/3 pyramidal neurons exhibited a greater degree of time-dependent rectification during somatic hyperpolarizing voltage responses (Supplementary Fig. 4a), as has previously been described [43], and showed a pronounced crossover in the decay phase of sEPSPs simultaneously recorded at dendritic site of generation and the soma, a hallmark of non-uniform membrane conductance [41,42] (Fig. 2a, Supplementary Fig. 3a). Furthermore, the resting membrane potential of HL2/3 pyramidal neurons was found to be significantly depolarized with respect to RL2/3 pyramidal neurons (Supplementary Fig. 4b). The pharmacological blockade of HCN channels, with ZD 7288 (10 μM) [41,42], powerfully hyperpolarized the resting membrane potential of HL2/3 pyramidal neurons, increased the apparent input resistance, and abolished the normalization of sEPSP time-course and summation (Supplementary Fig. 3). Taken

together these findings indicate that a constraint of EPSP time-course and temporal summation, coupled with the larger physical length of the apical dendritic tree of HL2/3 pyramidal neurons, limits the direct impact that dendritic excitatory input has at the axonal site of AP generation [44], suggesting that apical dendritic excitatory synaptic input may be locally integrated, and signaled into neuronal output by the generation of dendritic electrogenesis.

Phylogenetically conserved apical dendritic spike generation

As a first step to explore the electrical excitability of the dendritic tree of human and rat L2/3 pyramidal neurons we examined the properties of AP backpropagation (Fig. 3). Notably, the properties of somatically recorded APs were distinct between rat and human L2/3 pyramidal neurons, but were similar between HL2/3 pyramidal neurons recorded from tissues obtained from patients who had undergone neurosurgery for the alleviation of refractory epilepsy or the removal of sub-cortical brain tumours (Supplementary Fig. 5a-e). Simultaneous dendritic recordings revealed that somatic current step-evoked APs backpropagated into the apical dendritic tree (Fig. 3a,b). In RL2/3 pyramidal neurons, the amplitude of backpropagating APs (BPAPs) monotonically decreased, and the time-delay between somatic APs and BPAPs increased as dendritic recordings were made from increasingly distal sites (linear fit: conduction velocity= 0.21 m/s, r^2= 0.90, n= 37; Fig. 3c,d, black open symbols, full line). In contrast, in HL2/3 pyramidal neurons the distance-dependent pattern of AP backpropagation was more heterogeneous (Fig. 3c). In distal apical dendritic recordings, a fraction of HL2/3 pyramidal neurons exhibited BPAPs that appeared to follow the distance-dependent pattern of BPAP attenuation recorded from RL2/3 pyramidal neurons, whereas others exhibited larger amplitude BPAPs (Fig. 3c, black symbols, extrapolated fit to rat data shown as a dashed line). This heterogenous pattern of AP backpropagation was unrelated to the properties of somatically recorded APs, or etiology, as both weak and strong BPAPs were observed in neurons obtained from epileptic or tumour resection surgeries (Supplementary Fig. 5f,g). Despite this heterogeneity, APs backpropagated into the apical dendritic tree of HL2/3 pyramidal neurons with a conduction velocity of 0.23 m/s, similar to that of RL2/3 pyramidal neurons (linear fit, r^2= 0.87, n= 65; Figure 3a,d, filled black symbols).

Next, we directly examined apical dendritic electrical excitability by injecting incremental series of positive current steps through dendritic recording electrodes until a threshold (rheobase) regenerative response was generated. In recordings made from proximal apical sites, the injection of rheobase dendritic positive current steps directly drove AP firing in human and rat L2/3 pyramidal neurons (<150 μm from the soma; current step duration= 1 s; Fig. 3, positive times indicate that APs preceded BPAPs). In contrast, when recordings were made from more distal sites of HL2/3 pyramidal neurons, dendritic positive current steps typically evoked, as a threshold response, all-or-none dendritic spikes, which overshot 0 mV and preceded and drove AP firing following their forward propagation to the soma and axon (Fig. 3, negative times indicate dendritic spikes preceding APs, the amplitude of dendritic events was measured at the time of AP initiation). In dendritic recordings made at sites > 200 μm from the soma, dendritic spikes were generated as a threshold response in 22 of 35 HL2/3 pyramidal neurons examined (Fig. 3d). In these neurons the dendritic current required to initiate dendritic spikes, and consequentially AP output, was only marginally greater than the rheobase current required to directly generate AP firing when injected at the soma (dendrite rheobase: 0.56 ± 0.03 nA; soma rheobase= 0.50 ± 0.03 nA; distance from soma: 276 ± 9 μm). Notably, when AP firing was driven by dendritic spikes, somatically recorded APs were initiated from relatively negative membrane potentials, with a threshold that was significantly hyperpolarized in comparison to those evoked by somatic excitatory input (t-test, df= 24, P< 0.0001; Fig. 3a,f). Furthermore, dendritic spike generation in HL2/3 pyramidal neurons was sustainable across a wide dendritic current step range, and reliably drove AP output when the magnitude of dendritic current steps was increased to values up to 2 times the threshold current intensity (Fig. 3g,h). In contrast, in RL2/3 pyramidal neurons the presentation of long threshold steps of dendritic current evoked dendritic spike initiation in only one recording (Fig. 3d). Taken together these data reveal that the apical dendrites of HL2/3 pyramidal neurons are highly electrically excitable, and capable of generating powerful dendritic spikes. Our findings do not, however, directly show that apical dendritic excitability is enhanced in HL2/3 pyramidal neurons, as central neurons are not physiologically driven by long steps of current. We therefore explored if more physiological EPSP-shaped patterns of dendritic excitatory input [10] led to the initiation of dendritic spikes in human and rat L2/3 pyramidal neurons.

To our surprise we found that dendritic spikes were generated in response to threshold EPSP-shaped current waveforms in both HL2/3 and RL2/3 pyramidal neurons (τ_{rise}= 0.5 ms; τ_{decay}= 5 ms; Figs. 4 and 5). The presentation of single threshold sEPSPs, even at relatively proximal dendritic sites, typically led to the initiation of stereotyped dendritic spikes in human and rat L2/3 pyramidal neurons, which forward propagated to the soma and axon to drive AP firing (Fig. 4a-d). Analysis demonstrated that at apical dendritic sites >100 μm from the soma, dendritic spikes typically led and drove AP firing in both species (Fig. 4e), to produce a timing relationship of regenerative activity that was distinct from the relationship evoked by threshold somatic sEPSPs, which simply reflected the progressive time delay between APs and dendritic BPAPs (Fig. 4e). In common with dendritic spikes generated in response to long current steps, the voltage threshold for AP initiation, recorded at the soma, was significantly hyperpolarized when APs were driven by dendritic spikes in both human and rat L2/3 pyramidal neurons (human: dendritic EPSP driven= -62.8 ± 1.1 mV, soma EPSP driven= -50.6 ± 0.6 mV, t-test, df= 22, P< 0.0001; rat: dendritic EPSP driven= -60.1 ± 1.0 mV, soma EPSP driven= -52.3 ± 0.8 mV, t-test, df= 15, P< 0.0001; Fig. 4f). To examine the factors underlying this, we calculated the first derivative of somatically recorded APs, finding that dendritic spike initiation led to the generation of a ramp-like component which preceded the rapid upstroke of the first derivative of APs, a component that was absent when APs were driven by somatic sEPSPs in human and rat L2/3 pyramidal neurons, and so reflects the somatic impact of forward propagating dendritic spikes (Fig. 4g). Notably, the generation of dendritic spikes by sEPSPs was not simply a threshold mechanism, but was sustainable across a wide range of suprathreshold excitatory input, with grouped data showing a flat relationship between the peak voltage of dendritic spikes and the amplitude of the underlying simulated synaptic current in human and rat L2/3 pyramidal neurons (Fig. 4h), an input range over which dendritic spikes reliably preceded and drove AP output (Fig. 4i). These data therefore demonstrate that apical dendritic spike generation in human and rat L2/3 pyramidal neurons does not exhibit anti-coincidence properties.

We next explored if dendritic spikes could be generated repetitively. To do so we presented trains of sEPSPs at dendritic and somatic recording sites (inter-event interval 20 ms; Fig. 5). In both human and rat L2/3 pyramidal neurons the injection of threshold sEPSP trains at dendritic sites >100 μm from the soma led to the initiation

of dendritic spikes, which were characteristically generated late in the sEPSP train (Fig. 5a, Supplementary Fig. 5). At threshold, dendritic spikes forward propagated to drive AP output, yielding a distance-dependent timing relationship distinct from that generated by the generation of threshold sEPSP trains at the soma (Fig. 5b, Supplementary Fig. 6). Remarkably, when the amplitude of excitatory input was increased, dendritic spikes could be generated at high frequencies (Fig. 5a). Analysis revealed that in the majority of human and rat L2/3 pyramidal neurons dendritic spikes crowned the peak of each sEPSP of the train, and subsequently drove AP firing (Fig. 5a,d,e, Supplementary Fig. 6). In a fraction (<25 %) of HL2/3 pyramidal neurons, however, dendritic spike generation in response to the first sEPSP of a train failed to drive AP output, but was detectable at the soma as a subthreshold spikelet (Fig. 5a,c). This suppression of neuronal output was, however, transient, as dendritic spikes generated later in sEPSP trains reliably forward propagated to initiate AP output (Figure 5a,b,d). Indeed, pooled data revealed that active dendritic synaptic integration of sEPSP trains was operational across a wide input range, with dendritic spikes evoked at current intensities up to 4-fold greater than threshold (Fig. 5f,g). Over this input range 2021 of 2414 APs were driven by dendritic spikes, with grouped data showing a clear difference from the timing of regenerative activity evoked by the presentation of somatic sEPSP trains over a similar range (Fig. 5f,g). Taken together therefore, these data demonstrate that apical dendritic spikes are reliably and repetitively generated across a wide range of excitatory input, suggesting that the dendritic integrative properties of both human and rat L2/3 pyramidal neurons efficiently implement a correlative computation.

To further examine the frequency-following capacity of dendritic spikes in L2/3 pyramidal neurons we injected series of short (3 ms) threshold positive current steps at distal dendritic recording sites (Fig. 6). In both human and rat L2/3 pyramidal neurons dendritic spikes could be initiated and drive AP firing in response to dendritic positive current steps delivered at intervals as short as 10 ms (Fig. 6a,b). This frequency-following capacity mirrored the generation of AP firing evoked in response to short somatic positive current steps (Fig. 6a,b), suggesting that dendritic spikes and APs are mediated by similar classes of voltage-gated ion channels. To test this idea, we locally and transiently applied the sodium channel blocker tetrodotoxin (TTX) to a site close to the dendritic recording electrode (2 μM; pipette separation <20 μm; Fig.

6e,f). Under control conditions dendritic spikes robustly forward propagated to drive AP firing in HL2/3 pyramidal neurons; however, following the local dendritic application of TTX, dendritic spike generation was eliminated, and could not be restored by increasing the amplitude of positive current steps (Fig. 6e). This effect of dendritic sodium channel blockade was fully reversible and confined to dendritic sites, as the somatic amplitude of APs generated in response to short somatic current steps was unperturbed (Fig. 6e,f). Furthermore, the bath application of TTX (0.5-1 μM) abolished dendritic spikes evoked by short (3-5 ms) and long (1 s) positive dendritic current steps, as well as single and trains of sEPSPs (Supplementary Fig. 7a-d), revealing, by subtraction, that dendritic spikes in HL2/3 pyramidal neurons had an amplitude of 40.7 ± 2.4 mV and exhibited fast rise and decay kinetics (10-90 % rise time= 0.70 ± 0.07 ms; half-width= 1.51 ± 0.16 ms; n= 14; Supplementary Fig. 7d). Similarly, in RL2/3 pyramidal neurons, dendritic spikes were found to be mediated by dendritic TTX-sensitive sodium channels and possessed comparable properties (amplitude= 52.6 ± 2.2 mV; 10-90 % rise time= 0.53 ± 0.04 ms; half-width= 1.46 ± 0.10 ms; n= 7; Supplementary Fig. 7d-f). Taken together, these data reveal that dendritic spikes in human and rat L2/3 pyramidal neurons are mediated by the regenerative activation of dendritic sodium channels.

To explore if dendritic excitatory input to human and rat L2/3 pyramidal neurons could evoke regenerative dendritic activity following the pharmacological blockade of sodium channels, we generated families of large amplitude sEPSPs, and positive voltage steps, in the presence of TTX (Supplementary Figs. 7c and 8). Under these conditions dendritic excitatory input did not evoke regenerative activity, despite the generation of intense dendritic depolarization (Supplementary Figs. 7c and 8). We noted, however, that such input-output relationships were highly rectified in both species, suggesting that voltage-gated potassium channels regulate dendritic electrical excitability (Supplementary Fig. 8 a-c, f,g). Consistent with this idea, bath application of the potassium channel blocker 4-amino pyridine (5 mM), in TTX, was found to unmask apical dendritic electrogenesis generated in response to dendritic sEPSPs or positive current steps, which was largest in amplitude and peaked first at dendritic recording sites, and decrementally spread to the soma (Supplementary Fig. 8a-g). This dendritic regenerative activity could be pharmacologically blocked by the application of the non-specific calcium channel antagonist cadmium (100 μM, n= 5 HL2/3 pyramidal neurons;

Supplementary Fig. 8d,e). Notably, dendritic calcium spikes in HL2/3 pyramidal neurons recorded under these conditions discharged repetitively throughout the course of long dendritic positive current steps, and exhibited amplitudes similar to the dendritic calcium APs previously reported for HL2/3 pyramidal neurons under control conditions [22] (cadmium subtracted dendritic calcium spike: dendrite= 30.9 ± 6.6 mV (range= 24.8 - 40.4 mV), soma= 23.4 ± 4.2 mV n= 5 neurons). Therefore, consistent with observations made from other neuronal classes [25,45], our findings demonstrate that the expression of dendritic calcium electrogenesis is powerfully controlled by the activation of voltage-gated potassium channels in human and rat L2/3 pyramidal neurons.

In other central neurons a commonality between the generation mechanisms of APs and dendritic spikes has been shown to limit the temporal dynamics of active dendritic integration, as reliance on the same classes of ion channel can lead to use-dependent inactivation [46]. To explore the time-window over which AP output influences dendritic sodium spike generation in HL2/3 pyramidal neurons we generated AP firing by the presentation of short somatic current pulses, and at subsequent times probed for the generation of dendritic spikes by the delivery of threshold dendritic positive current steps (Fig. 6c,d). To our surprise AP firing and subsequent AP backpropagation only precluded dendritic integration over a very narrow time-window (<10 ms), after which dendritic spikes were reliably generated and forward propagated to drive AP output (Fig. 6c,d). Thus, in human and rat L2/3 pyramidal neurons dendritic spikes signal, at high repetition frequencies, the result of dendritic integration, but how precisely do dendritic spikes drive neuronal output? To address this, we generated dendritic spikes in response to short threshold positive current steps and measured the time-delay between the peak of dendritic spikes and somatically recorded APs across multiple trials (Fig. 6g,h). Pooled data revealed that the forward propagation of dendritic spikes was reliable and drove time-locked AP firing, exhibiting little trial-to-trial temporal jitter (half-width of the temporal jitter around mean: HL2/3= 61 μs; RL2/3= 41 μs; Fig. 6g,i). This temporal precision emerged in HL2/3 pyramidal neurons despite the relatively long-time delay incurred by the forward propagation of dendritic spikes from site of generation to the axon (Fig. 6i). Taken together therefore, our findings reveal that a phylogenetic conserved mechanism signals the result of dendritic computations into AP output in human and rat L2/3 pyramidal neurons.

Discussion

Here we demonstrate the mechanistic and functional conservation of the properties of active dendritic integration in human and rodent L2/3 neocortical pyramidal neurons. Our findings do not, however, support conservative scaling principles, which posit that the electrical architecture of neuronal classes are conserved between species [47]. This arises because voltage attenuation in the apical dendritic tree of L2/3 pyramidal neurons was found to exhibit similar distance-dependent properties between species, and so the electrical architecture of HL2/3 pyramidal neurons is more distributed, reflecting the greater physical length of apical dendritic tree. Such a finding is noteworthy, as previous computational modeling has suggested that the dendritic cable properties of human L2/3 pyramidal neurons are distinct from those of the rodent, due to unique capacitive properties of the plasma membrane [39]. However, our simultaneous recordings, and direct measurement of membrane capacitance do not support such a species-specific adaptation, a finding underscored by observations made from HL5 pyramidal neurons [24]. In contrast, we find that the electrical and morphological distribution of the dendritic tree provides a foundation for the enhanced emergence of independent integrative compartments in HL2/3 pyramidal neurons. At these sites, dendritic excitatory input is integrated to form dendritic sodium spikes, which forward propagate to drive neuronal output across a wide range of correlated excitatory input, consistent with computational models which describe the dendritic integrative operations of rodent pyramidal neurons as two-layered neural networks [9,32,33]. As neuronal modeling has suggested that dendritic sodium spikes of rodent L2/3 pyramidal neurons are driven by the strongest 1% of excitatory synaptic inputs, and by the activation of spatially clustered excitatory input [28], it is tempting to speculate that the increased number of dendritic spines in HL2/3 pyramidal neurons [3,5,6] provides an increased substrate for such dendritic computations.

In both human and rat L2/3 pyramidal neurons, dendritic sodium spikes could be generated at high frequencies, exhibiting characteristics similar to those recorded in isolation from the thin apical dendrites of rodent neocortical pyramidal neurons *in vivo* using invasive and non-invasive recording techniques [14,19], and other neuronal classes [30,35,36]. However, such properties are mechanistically and functionally distinct from the pattern of apical dendritic excitability recently reported for HL2/3 pyramidal neurons,

characterized by the generation of calcium channel-mediated dendritic APs [22], which inactivate upon increased excitatory drive to implement a novel anti-coincidence computation. Although we have no explanation for such a profound difference in the active dendritic integration operations of HL2/3 pyramidal neurons between studies, as recordings were made under similar conditions from the same cortical area. It is possible that through the evolutionary expansion of the human neocortex, neuronal classes with distinct properties have emerged, as highlighted by the existence of a sparse population of molecularly unique layer 3 pyramidal neurons in the human [4]. On the other hand, our observation that the pharmacological blockade of voltage-gated potassium channels unmasks dendritic calcium electrogenesis in human and rat L2/3 pyramidal neurons, consistent with previous findings made from other neuronal classes in the rodent neocortex [25,45], suggests that differences between our and previous work [22] may, in part, be explained by the differential regulation of potassium channel function. Consistent with this idea, the membrane expression and voltage-dependent availability of voltage-gated potassium channels is known to be controlled by a variety of factors such as neuronal activity [48-50], osmolarity [51], intracellular calcium [52], and neuromodulators [53], and so may have been down-regulated in previous investigation of HL2/3 pyramidal neurons [22]. Notwithstanding, our observation of the conservation of suprathreshold dendritic integrative operations, biophysical constants, and dendritic cable properties between L2/3 pyramidal neurons of the human and rodent neocortex is consistent with the predominant molecular conservation of supragranular pyramidal neurons in these species [4]. Thus, we suggest that the enlargement and complexification of the dendritic tree of human L2/3 pyramidal neurons provides an enhanced framework for the execution of phylogenetically conserved dendritic computational operations, which are translated into neuronal output by the high-fidelity generation and forward propagation of dendritic sodium spikes.

Methods

Human brain slice preparation

Males or females aged 17-70 years (median 42 years) who provide informed written consent for the provision of normative tissue surplus to diagnostic requirements (normative tissue) were admitted to the study. All clinical, experimental, and administrative procedures were approved by the Mater Misericordiae Ltd. Human Research Ethics Committee (HREC/MML/63124) and ratified by the The University of Queensland. Patients undergoing neurosurgery were maintained under general anesthesia following neuro-muscular blockade (Supplementary Tables 1 and 2). Brain tissue was resected typically less than 1 h after the start of the procedure and was considered surplus normative tissue. Normative tissue did not demonstrate abnormalities at the level of preoperative magnetic resonance imaging (MRI) or during neurosurgical resection and was not subjected to clinical pathological analysis. In refractory epilepsy cases, the epileptogenic zone (EZ) was identified by anatomoelectroclinical correlations. If there was discordance in these data, the EZ was localized by stereo-electroencephalography prior to resection (see Supplementary Table 1). Normative tissue adjacent to the EZ was resected, while tissue obtained from the EZ was subsequently resected and subjected to clinical pathological analysis (Supplementary Table 1). In tumour cases, the location of sub-cortical tumours was visualized by preoperative MRI and in some cases dynamically during neurosurgery with the use of optical imaging agents (Supplementary Table 2). In all cases the resected tissue provided was considered normative tissue during neurosurgery, whereas abnormal tissue was subjected to clinical pathological analysis (Supplementary Table 2). In all reported cases brain tissue was resected from the anterior temporal lobe (see Supplementary Tables 1 and 2). The resected brain tissue was immediately (<15 s) placed into a container and immersed in a saturated (95% O_2, 5% CO_2) ice-cold solution of the following composition: (in mM) sucrose 75, NaCl 87, KCl 2.5, $Na_2H_2PO_4$ 1.25, $NaHCO_3$ 25, glucose 10, Na pyruvic acid 3, $MgCl_2$ 3, $CaCl_2$ 0.5. The container was sealed, packed into a second vessel and placed on ice for transportation to the laboratory, where the tissue was removed and placed in fresh ice-cold saturated (95% O_2, 5% CO_2) solution of the same composition within 14-30 min of resection. The tissue block was then inspected, divided if necessary, and re-

blocked perpendicular to the cortical surface. We made no attempt to remove the remaining meninges from the surface of tissue blocks as preliminary evidence suggested that such mechanical disturbance impacted the morphology of the fine-calibre apical tuft dendrites of pyramidal neurons. Tissue blocks were adhered to the stage of a vibrating blade microtome and rapidly immersed in the same ice-cold solution after which 300-350 μm brain slices were prepared. Each brain slice was then immediately transferred to a storage chamber filled with a solution of composition (in mM): NaCl 92, KCl 2.5, $Na_2H_2PO_4$ 1.2, $NaHCO_3$ 30, HEPES 20, glucose 20, Na-L-ascorbate 5, Na pyruvic acid 3, thiourea 2; $MgCl_2$ 10, $CaCl_2$ 0.5, saturated with 95% O_2, 5% CO_2 at 34-36^oC for 30 min. Brain slices were then individually transferred to storage chambers filled with a saturated (95% O_2, 5% CO_2) solution of composition (in mM): NaCl 125, KCl 2.5, $Na_2H_2PO_4$ 1.25, $NaHCO_3$ 25, glucose 25, Na pyruvic acid 3, $MgCl_2$ 6, $CaCl_2$ 1 and maintained at room temperature (20-24 ^oC).

Rat brain slice preparation

All experiments were approved by the Animal Ethics Committee of The University of Queensland in accordance with the Australian Code of Practice for the Care and Use of Animals for Scientific Purposes. Wistar rats (male, P30 - P45) were deeply anesthetized by inhalation of isoflurane and decapitated. Brain slices (300 μm) including the temporal associative area, with reference to [54] were cut in the coronal plane in an ice-cold solution of composition (in mM): sucrose 75, NaCl 87, KCl 2.5, $Na_2H_2PO_4$ 1.25, $NaHCO_3$ 25, glucose 10, Na pyruvic acid 3, $MgCl_2$ 3, $CaCl_2$ 0.5. Brain slices were then immediately transferred to a storage chamber filled with a saturated (95% O_2, 5% CO_2) solution of composition (in mM): NaCl 125, KCl 2.5, $Na_2H_2PO_4$ 1.25, $NaHCO_3$ 25, glucose 25, Na pyruvic acid 3, $MgCl_2$ 6, $CaCl_2$ 1 at 34-34^oC for 30 min, and maintained at room temperature.

Electrophysiological recordings

Individual brain slices were placed in a chamber perfused with a constant flow of artificial cerebral spinal fluid (ACSF) of composition (in mM): NaCl 125, $NaHCO_3$ 25, KCl 2.5, NaH_2PO_4 1.25, 1 $CaCl_2$ 1, $MgCl_2$ 1, Na pyruvic acid 3 and glucose 25 saturated with 95 % O_2 and 5 % CO_2 at 35-36.5 °C. In the majority of experiments, spontaneous synaptic activity was blocked by the addition of CNQX (10 μM, Tocris), DL-AP5 (50 μM, Tocris), SR 95531 (5 μM, Tocris), and CGP52432 (10 μM, Tocris).

The ion channel blockers ZD7288 (10 μM, Tocris), cadmium chloride (100 M, Merck), 4-amino pyridine (5mM, Merck) and TTX (0.5-1 μM, Alomone) were added to the extracellular solution when indicated. In some experiments TTX (2 μM, dissolved in saturated ACSF) was applied close to the site (<20 μm) of dendritic recording by pressure application (20 to 30 s) from a pipette with characteristics similar to those used for dendritic whole-cell recordings. Recordings were made from pyramidal neurons identified by their soma shape and ascending apical dendrite projecting to layer 1, when visualized with video-enhanced infra-red differential interference contrast microscopy. Dual whole-cell, current-clamp recordings were made with identical dedicated current-clamp amplifiers (BVC 700A; Dagan). The electrode capacitance and series resistance was compensated using the active circuitry of the amplifier. Pipettes were filled with a solution containing (in mM): K-gluconate 135, NaCl 7, HEPES 10, Na_2ATP 2, NaGTP 0.3, 2 MgCl, Na_2Phosphocreatine 10, and Alexa Fluor 598 0.01, pH 7.2 - 7.3, for somatic (open tip resistance 3-6 MΩ) and dendritic (open tip resistance 10-15 MΩ) recordings. Somatic or dendritic recordings were rejected if the series resistance exceeded 20 or 70 MΩ, respectively. Signals were lowpass filtered (DC to 10 kHz) and acquired by Axograph software at 50-100 kHz. At the termination of each recording, neuronal morphology and the placement of recording electrodes were recorded by fluorescence microscopy (QImaging). For nucleated patch recording, pipettes which had an open tip resistance of 2-4 MΩ when filled with the above internal solution were used to form high seal-resistance cell-attached recordings from visually identified pyramidal neurons, and the pipette capacitance was fully compensated. On successful excision of a nucleated patch, the patch was raised above the brain slice to the level of a prepositioned sylgard ball formed at the tip of a second pipette controlled by an independent manipulator. Current responses, recorded with a multi-clamp 700B amplifier (Molecular Devices), were evoked from a holding potential of -70 mV by the repeated delivery of voltage command steps (1000 repetitions, -5 mV, 7 ms). Recordings were lowpass filtered (DC to 30 kHz) and sampled at high frequency (250 kHz). High-resolution (60 x objective, 4 x optical magnification) photomicrographs were taken of each nucleated patch, allowing measurement of the major and minor axes and the calculation of surface area [40]. At the termination of each recording the patch was ruptured, blown from the mouth of the pipette, and the recording pipette positioned to touch the sylgard ball where a

high-resistance seal was formed. The voltage protocol was then repeated. The digital averages of current responses under these conditions were subtracted to remove any uncompensated residual pipette capacitance [40]. Experimental data were analyzed using Axograph, GraphPad Prism, SigmaPlot and Microsoft Excel. The voltage threshold of AP initiation was calculated as the point when the first derivative of somatically recorded APs exceeded 15 V.s. The recorded membrane potential values were adjusted for pipette offset, but not liquid junction potential.

Microscopy and neuronal reconstruction

For accurate reconstruction, pyramidal neurons were filled with 0.5 % biocytin (wt / vol, 5 mg / ml, Sigma) and slices fixed in 4 % paraformaldehyde (pH 7.3 - 7.4) for 12 h. The slices were then reacted with 0.1 % streptavidin conjugated with Alexa Fluor-568 (Invitrogen) and 0.1 % Triton X-100 for 12 h at room temperature. Slices were subsequently reacted with DAPI (0.02 % in saline) for 30 min at room temperature, and then mounted and cover-slipped with Aqua Polymount (Polysciences) or Vectashield (Vector Laboratories). Optically sectioned (0.5 μm z step size) x-y photomicrograph montages of neuronal morphology were acquired using an inverted spinning-disk confocal microscope, either a W1 Yokogawa spinning disk module (3i), Zeiss Axio Observer Z1 microscope, Hamamatsu Flash4 sCMOS camera, and 40 x 1.2 NA C-Apochromat water immersion objective, or a Diskovery spinning disk module, Nikon TiE microscope, Zyla 4.2 sCMOS camera, and 40 x 1.15 NA Plan-Apochromat water immersion objective. Photomicrographs were acquired using 1 x 1 binning, with an exposure of 200-450 ms, set to allow the greatest dynamic range for all processes while not being so long as to over-bleach the fluorophore. Neurons were reconstructed manually and/or semi-automatically using a user-guided algorithm with Neurolucida 360 (MicroBrightField) at high digital magnification in 3 dimensions, and the reconstructions visualized and analyzed with Neurolucida Explorer (MicroBrightField) software. Neurons possessing dendritic trees that appeared substantially truncated by the slicing procedure were excluded from further analysis. Dendritic diameter was measured using Neurolucida 360, where apical dendritic segments were semi-automatically traced with the user-guided rayburst crawl algorithm. For proximal apical dendrite segments, the segment began 15 μm from the centre of the soma and continued for 20 μm. For distal apical segments (20 μm), the segment began 20 μm proximal to the main bifurcation of the apical dendrite (the

nexus). Basal dendritic segments were manually traced to the first branch point or if a measured basal dendrite did not branch, it was measured for 20 μm or to termination, whichever was shorter. Traced segments were then loaded into Neurolucida Explorer and the average thickness of each segment calculated. For HL2/3 pyramidal neurons we also measured the average diameter of the distal 10 μm of proximal apical dendritic segments, to eliminate possible distortion of the diameter imposed by measurement of the soma-dendritic border. For illustrative purposes only, dendritic processes of reconstructions were thickened in Adobe Illustrator in order to provide clarity in text figures.

Other statistics

No strategy for randomization and/or stratification was adopted. It was not possible to perform this study blinded. Inclusion and exclusion criteria for individual data types are detailed below.

Values reported are mean ± standard error of the mean (S.E.M.), unless otherwise stated, and n values represent the number of cells, unless otherwise stated. Statistical significance was defined when the probability of the data being observed under a null hypothesis was less than an alpha level of 0.05. Significance was tested with a two-tail Students' t-test, with Welch's correction being used for samples with unequal variance. The Mann Whitney test was used as a non-parametric test. Details of statistical tests can be found in the Results section. Statistical analysis was carried out using Prism 9 (Graphpad).

Only supragranular pyramidal neurons were included in the analysis. The laminar position of each neuron was determined by the merging of fluorescence images of biocytin-filled neurons with the nuclear counterstain DAPI, which was used to define neocortical lamination. Somatic or dendritic electrophysiological recordings were rejected if the somatic series resistance changed by >15 % during the experiment, or the dendritic series resistance changed by >40 %, or exceeded 20 or 70 MΩ, respectively. Recordings were also rejected if the observed recordings were highly unstable, or if neurons had a membrane potential that was depolarized relative to the norm.

References

1 Miller, I. F., Barton, R. A. & Nunn, C. L. Quantitative uniqueness of human brain evolution revealed through phylogenetic comparative analysis. *Elife* **8**, doi:10.7554/eLife.41250 (2019).
2 Glasser, M. F. *et al.* A multi-modal parcellation of human cerebral cortex. *Nature* **536**, 171-178, doi:10.1038/nature18933 (2016).
3 DeFelipe, J., Alonso-Nanclares, L. & Arellano, J. I. Microstructure of the neocortex: comparative aspects. *J Neurocytol* **31**, 299-316, doi:10.1023/a:1024130211265 (2002).
4 Hodge, R. D. *et al.* Conserved cell types with divergent features in human versus mouse cortex. *Nature* **573**, 61-68, doi:10.1038/s41586-019-1506-7 (2019).
5 Elston, G. N., Benavides-Piccione, R. & DeFelipe, J. The pyramidal cell in cognition: a comparative study in human and monkey. *J Neurosci* **21**, Rc163, doi:10.1523/JNEUROSCI.21-17-j0002.2001 (2001).
6 Shapson-Coe, A. *et al.* A connectomic study of a petascale fragment of human cerebral cortex. *bioRxiv*, 2021.2005.2029.446289, doi:10.1101/2021.05.29.446289 (2021).
7 Larkum, M. E., Zhu, J. J. & Sakmann, B. A new cellular mechanism for coupling inputs arriving at different cortical layers. *Nature* **398**, 338-341, doi:10.1038/18686 (1999).
8 Williams, S. R. & Stuart, G. J. Dependence of EPSP efficacy on synapse location in neocortical pyramidal neurons. *Science* **295**, 1907-1910, doi:10.1126/science.1067903 (2002).
9 London, M. & Häusser, M. Dendritic computation. *Annu Rev Neurosci* **28**, 503-532, doi:10.1146/annurev.neuro.28.061604.135703 (2005).
10 Larkum, M. E., Waters, J., Sakmann, B. & Helmchen, F. Dendritic spikes in apical dendrites of neocortical layer 2/3 pyramidal neurons. *J Neurosci* **27**, 8999-9008, doi:10.1523/jneurosci.1717-07.2007 (2007).
11 Williams, S. R. & Fletcher, L. N. A dendritic substrate for the cholinergic control of neocortical output neurons. *Neuron* **101**, 486-499, doi:10.1016/j.neuron.2018.11.035 (2019).
12 Lavzin, M., Rapoport, S., Polsky, A., Garion, L. & Schiller, J. Nonlinear dendritic processing determines angular tuning of barrel cortex neurons in vivo. *Nature* **490**, 397-401, doi:10.1038/nature11451 (2012).
13 Xu, N. L. *et al.* Nonlinear dendritic integration of sensory and motor input during an active sensing task. *Nature* **492**, 247-251, doi:10.1038/nature11601 (2012).
14 Smith, S. L., Smith, I. T., Branco, T. & Häusser, M. Dendritic spikes enhance stimulus selectivity in cortical neurons in vivo. *Nature* **503**, 115-120, doi:10.1038/nature12600 (2013).
15 Palmer, L. M. *et al.* NMDA spikes enhance action potential generation during sensory input. *Nat Neurosci* **17**, 383-390, doi:10.1038/nn.3646 (2014).
16 Stuart, G. J. & Spruston, N. Dendritic integration: 60 years of progress. *Nat Neurosci* **18**, 1713-1721, doi:10.1038/nn.4157 (2015).
17 Takahashi, N., Oertner, T. G., Hegemann, P. & Larkum, M. E. Active cortical dendrites modulate perception. *Science* **354**, 1587-1590, doi:10.1126/science.aah6066 (2016).

18 Schmidt-Hieber, C. *et al.* Active dendritic integration as a mechanism for robust and precise grid cell firing. *Nat Neurosci* **20**, 1114-1121, doi:10.1038/nn.4582 (2017).
19 Moore, J. J. *et al.* Dynamics of cortical dendritic membrane potential and spikes in freely behaving rats. *Science* **355**, eaaj1497, doi:10.1126/science.aaj1497 (2017).
20 Beaulieu-Laroche, L., Toloza, E. H. S., Brown, N. J. & Harnett, M. T. Widespread and highly correlated somato-dendritic activity in cortical layer 5 neurons. *Neuron* **103**, 235-241, doi:10.1016/j.neuron.2019.05.014 (2019).
21 Suzuki, M. & Larkum, M. E. General anesthesia decouples cortical pyramidal neurons. *Cell* **180**, 666-676, doi:10.1016/j.cell.2020.01.024 (2020).
22 Gidon, A. *et al.* Dendritic action potentials and computation in human layer 2/3 cortical neurons. *Science* **367**, 83-87, doi:10.1126/science.aax6239 (2020).
23 Beaulieu-Laroche, L. *et al.* Allometric rules for mammalian cortical layer 5 neuron biophysics. *Nature*, 10.1038/s41586-41021-04072-41583, doi:10.1038/s41586-021-04072-3 (2021).
24 Beaulieu-Laroche, L. *et al.* Enhanced dendritic compartmentalization in human cortical neurons. *Cell* **175**, 643-651, doi:10.1016/j.cell.2018.08.045 (2018).
25 Harnett, M. T., Xu, N. L., Magee, J. C. & Williams, S. R. Potassium channels control the interaction between active dendritic integration compartments in layer 5 cortical pyramidal neurons. *Neuron* **79**, 516-529, doi:10.1016/j.neuron.2013.06.005 (2013).
26 Kim, H. G. & Connors, B. W. Apical dendrites of the neocortex: correlation between sodium- and calcium-dependent spiking and pyramidal cell morphology. *J Neurosci* **13**, 5301-5311, doi:10.1523/jneurosci.13-12-05301.1993 (1993).
27 Kalmbach, B. E. *et al.* Signature morpho-electric, transcriptomic, and dendritic properties of human layer 5 neocortical pyramidal neurons. *Neuron* **109**, 2914-2927.e2915, doi:10.1016/j.neuron.2021.08.030 (2021).
28 Goetz, L., Roth, A. & Häusser, M. Active dendrites enable strong but sparse inputs to determine orientation selectivity. *Proc Natl Acad Sci U S A* **118**, 10.1073/pnas.2017339118, doi:10.1073/pnas.2017339118 (2021).
29 Waters, J., Larkum, M., Sakmann, B. & Helmchen, F. Supralinear Ca2+ influx into dendritic tufts of layer 2/3 neocortical pyramidal neurons in vitro and in vivo. *J Neurosci* **23**, 8558-8567, doi:10.1523/jneurosci.23-24-08558.2003 (2003).
30 Losonczy, A., Makara, J. K. & Magee, J. C. Compartmentalized dendritic plasticity and input feature storage in neurons. *Nature* **452**, 436-441, doi:10.1038/nature06725 (2008).
31 Larkum, M. E., Nevian, T., Sandler, M., Polsky, A. & Schiller, J. Synaptic integration in tuft dendrites of layer 5 pyramidal neurons: a new unifying principle. *Science* **325**, 756-760, doi:10.1126/science.1171958 (2009).
32 Poirazi, P., Brannon, T. & Mel, B. W. Pyramidal neuron as two-layer neural network. *Neuron* **37**, 989-999, doi:10.1016/s0896-6273(03)00149-1 (2003).
33 Polsky, A., Mel, B. W. & Schiller, J. Computational subunits in thin dendrites of pyramidal cells. *Nat Neurosci* **7**, 621-627, doi:10.1038/nn1253 (2004).
34 Doron, G. *et al.* Perirhinal input to neocortical layer 1 controls learning. *Science* **370**, doi:10.1126/science.aaz3136 (2020).
35 Chen, W. R., Midtgaard, J. & Shepherd, G. M. Forward and backward propagation of dendritic impulses and their synaptic control in mitral cells. *Science* **278**, 463-467, doi:10.1126/science.278.5337.463 (1997).

36 Sivyer, B. & Williams, S. R. Direction selectivity is computed by active dendritic integration in retinal ganglion cells. *Nat Neurosci* **16**, 1848-1856, doi:10.1038/nn.3565 (2013).
37 Sheffield, M. E. & Dombeck, D. A. Calcium transient prevalence across the dendritic arbour predicts place field properties. *Nature* **517**, 200-204, doi:10.1038/nature13871 (2015).
38 Rall, W. Distinguishing theoretical synaptic potentials computed for different soma-dendritic distributions of synaptic input. *J Neurophysiol* **30**, 1138-1168, doi:10.1152/jn.1967.30.5.1138 (1967).
39 Eyal, G. *et al.* Unique membrane properties and enhanced signal processing in human neocortical neurons. *Elife* **5**, e16553, doi:10.7554/eLife.16553 (2016).
40 Gentet, L. J., Stuart, G. J. & Clements, J. D. Direct measurement of specific membrane capacitance in neurons. *Biophys J* **79**, 314-320, doi:10.1016/s0006-3495(00)76293-x (2000).
41 Williams, S. R. & Stuart, G. J. Site independence of EPSP time course is mediated by dendritic I(h) in neocortical pyramidal neurons. *J Neurophysiol* **83**, 3177-3182, doi:10.1152/jn.2000.83.5.3177 (2000).
42 Magee, J. C. Dendritic Ih normalizes temporal summation in hippocampal CA1 neurons. *Nat Neurosci* **2**, 508–514 doi:10.1038/12229 (1999).
43 Kalmbach, B. E. *et al.* h-channels contribute to divergent intrinsic membrane properties of supragranular pyramidal neurons in human versus mouse cerebral cortex. *Neuron* **100**, 1194-1208, doi:10.1016/j.neuron.2018.10.012 (2018).
44 Kole, M. H. *et al.* Action potential generation requires a high sodium channel density in the axon initial segment. *Nat Neurosci* **11**, 178-186, doi:10.1038/nn2040 (2008).
45 Yuste, R., Gutnick, M. J., Saar, D., Delaney, K. R. & Tank, D. W. Ca2+ accumulations in dendrites of neocortical pyramidal neurons: an apical band and evidence for two functional compartments. *Neuron* **13**, 23-43, doi:10.1016/0896-6273(94)90457-x (1994).
46 Remy, S., Csicsvari, J. & Beck, H. Activity-dependent control of neuronal output by local and global dendritic spike attenuation. *Neuron* **61**, 906-916, doi:10.1016/j.neuron.2009.01.032 (2009).
47 Wittenberg, G. M. & Wang, S. S. H. in *Dendrites* (eds G. Stuart, N. Spruston, & M. Hausser) 43-67 (Oxford University Press, 2007).
48 Frick, A., Magee, J. & Johnston, D. LTP is accompanied by an enhanced local excitability of pyramidal neuron dendrites. *Nat Neurosci* **7**, 126-135, doi:10.1038/nn1178 (2004).
49 Kim, J., Jung, S. C., Clemens, A. M., Petralia, R. S. & Hoffman, D. A. Regulation of dendritic excitability by activity-dependent trafficking of the A-type K+ channel subunit Kv4.2 in hippocampal neurons. *Neuron* **54**, 933-947, doi:10.1016/j.neuron.2007.05.026 (2007).
50 Sandler, M., Shulman, Y. & Schiller, J. A novel form of local plasticity in tuft dendrites of neocortical somatosensory layer 5 pyramidal neurons. *Neuron* **90**, 1028-1042, doi:10.1016/j.neuron.2016.04.032 (2016).
51 Caspi, A., Benninger, F. & Yaari, Y. KV7/M channels mediate osmotic modulation of intrinsic neuronal excitability. *J Neurosci* **29**, 11098-11111, doi:10.1523/jneurosci.0942-09.2009 (2009).
52 An, W. F. *et al.* Modulation of A-type potassium channels by a family of calcium sensors. *Nature* **403**, 553-556, doi:10.1038/35000592 (2000).

53 Hoffman, D. A. & Johnston, D. Downregulation of transient K+ channels in dendrites of hippocampal CA1 pyramidal neurons by activation of PKA and PKC. *J Neurosci* **18**, 3521-3528, doi:10.1523/jneurosci.18-10-03521.1998 (1998).
54 Paxinos, G. & Watson, C. *The rat brain in stereotaxic coordinates*. Vol. Sixth Edition (Elsevier, 2007).

Acknowledgements

We are grateful to Rowan Tweedal for comments on a previous draft of the manuscript, and Rumelo Amor, Andrew Thompson and Arnaud Gaudin for their help with procedures for the imaging and reconstruction of neurons. We are grateful to Sue Engstrom and Karen Campbell (Brisbane Clinical Neuroscience Centre) for their help with project logistics. We are particularly grateful to the patients for their very generous donation. This work was supported by the National Health and Medical Research Council of Australia (GA59869 to SRW). Imaging was performed at the Queensland Brain Institute's Advanced Microscopy Facility, generously supported by the Australian Government through the Australian Research Council LIEF grants LE100100074 and LE130100078.

Author Information:

Affiliations

Queensland Brain Institute, The University of Queensland; Brisbane, Queensland, Australia

Helen M. Gooch, Tobias Bluett, Lisa Gillinder, Madhusoothanan B. Perumal, Hong D. Vo, Lee N. Fletcher, Stephen R. Williams

Mater Centre for Neurosciences, Mater Hospital; Brisbane, Queensland, Australia

Damian Amato, Robert Campbell, Lisa Gillinder, Jason Papacostas, Jason McMillen, Tony Tsahtsarlis, Martin Wood

Royal Brisbane and Women’s Hospital; Brisbane, Queensland, Australia

Michael J. Colditz, Rosalind L. Jeffree

Contributions

Experimental: SRW, HMG, MBP and TB performed experiments. Analysis: SRW, HMG and MBP analysed electrophysiological data, HMG, TB, HDV, and LNF performed immunohistochemistry, confocal imaging, and neuronal reconstructions. Ethics and project management: LG and HMG. Surgery: JP, RLJ, MW, MJC, JM, TT, DA and RC provided human tissue. Conceptualization: SRW. Writing: SRW wrote the

original draft manuscript, all authors participated in writing, reviewing, and editing of the manuscript.

Corresponding author. Stephen R. Williams

Ethics declaration:

Competing interests

The authors declare no competing financial interests.

Data and availability:

All data are available in the main text and supplementary materials.

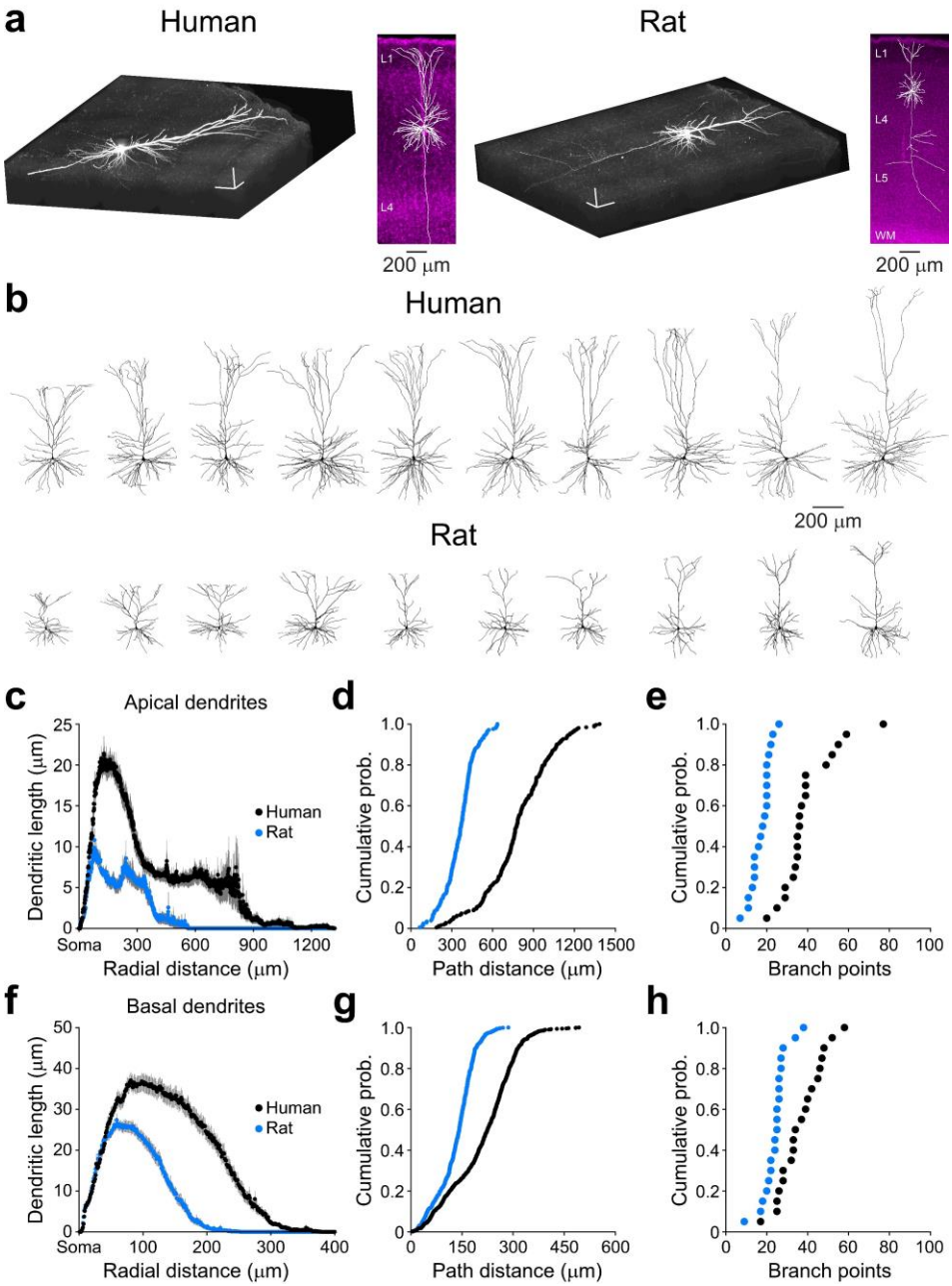

Figure 1. Morphological elaboration of the dendritic tree of human L2/3 pyramidal neurons

a, Volume representation of a biocytin-filled HL2/3 and RL2/3 pyramidal neuron. The scale bars represent 100 µm. The insets show reconstructions of the neurons (white) superposed onto low power fluorescence images of neocortical slices counterstained with the nuclear marker DAPI (magenta). The descending axons have been partly reconstructed. **b,** 2-dimensional projections of ten representative reconstructed human and rat L2/3 pyramidal neurons. **c,** Sholl analysis of the apical dendritic tree of HL2/3 (black symbols) and RL2/3 (blue symbols) pyramidal neurons (n= 20 neurons

in each species, grey lines represent ± S.E.M.). **d-e,** Cumulative probability distributions of path distance from soma to termination of apical dendrites (d) and the number of branch points in the apical dendritic tree (e). **f,** Sholl analysis of the basal dendritic tree of HL2/3 and RL2/3 pyramidal neurons. **g-h,** Cumulative probability distributions of path distance from soma to termination of basal dendrites (g) and the number of branch points in the basal dendritic tree (h).

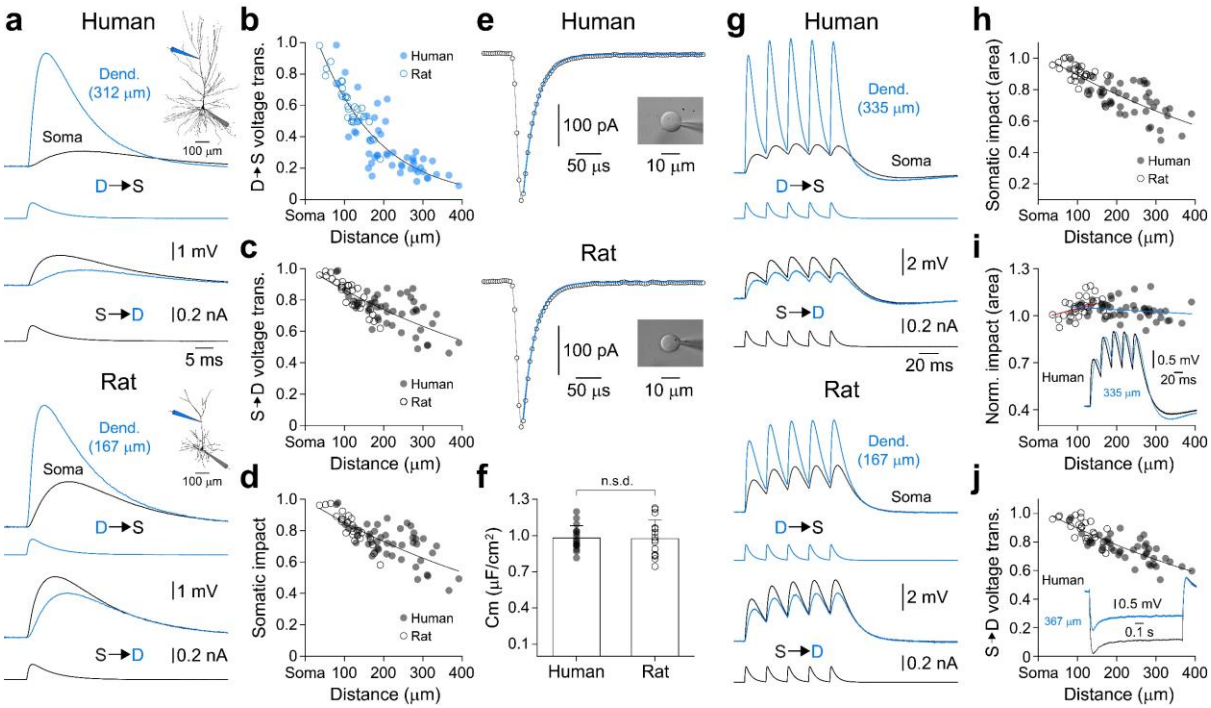

Figure 2. Voltage attenuation in the apical dendritic tree of human and rat L2/3 pyramidal neurons

a, Simultaneous dendritic (Dend., blue) and somatic (black) recording of simulated EPSPs (sEPSPs), showing dendro-somatic (D-S) and somato-dendritic (S-D) attenuation in human and rat L2/3 pyramidal neurons. The driving currents injected at dendritic and somatic sites are shown below voltage traces. The morphology of recorded neurons and placement of recording electrodes are inset. **b,** Distance-dependency of sEPSP dendro-somatic voltage transfer in HL2/3 (filled symbols) and RL2/3 (open symbols) pyramidal neurons. The line represents a single exponential fit, with a length constant of 154 μm. **c,** Distance-dependency of sEPSP somato-dendritic voltage transfer in human and rat L2/3 pyramidal neurons. The line represents a single exponential fit with a length constant of 641 μm. **d,** Somatic impact of dendritic sEPSPs, calculated by the division of the somatic amplitude of sEPSPs generated at the soma and apical dendritic sites. The line represents a single exponential fit with length constant of 642 μm. **e,** Charging patterns of nucleated patches excised from human and rat L2/3 pyramidal neurons. Each symbol shows a sampling point, and the blue lines represent single exponential fits to the data. Photomicrographs of the recorded human and rat nucleated patches are inset. **f,** Specific membrane capacitance of human and rat L2/3 pyramidal neurons are not significantly different

(n.s.d.), bars represent mean ± S.D. **g,** Simultaneous dendritic and somatic recordings of simulated EPSP trains, showing the pattern of D-S and S-D attenuation in a human and rat L2/3 pyramidal neuron. The driving currents injected at dendritic and somatic sites are shown below voltage traces. **h,** Somatic impact of the area of dendritic sEPSPs, calculated by the division of the somatic area of sEPSP trains generated at the soma and apical dendritic sites. The line represents a single exponential fit with a length constant of 679 μm. **i,** Somatic impact of dendritic sEPSP trains following normalization of the amplitude of the first sEPSP of the train in RL2/3 (open symbols) and HL2/3 (filled symbols) pyramidal neurons. Data have been fit by linear regression (rat, red line; human, blue line). The inset shows representative somatic recording of amplitude normalized sEPSP trains, generated at somatic and apical dendritic sites. **j,** Somato-dendritic peak voltage attenuation of negative voltage steps in human and rat L2/3 pyramidal neurons. The line represents a single exponential fit with a length constant of 708 μm. The inset shows a representative recording of a HL2/3 pyramidal neuron.

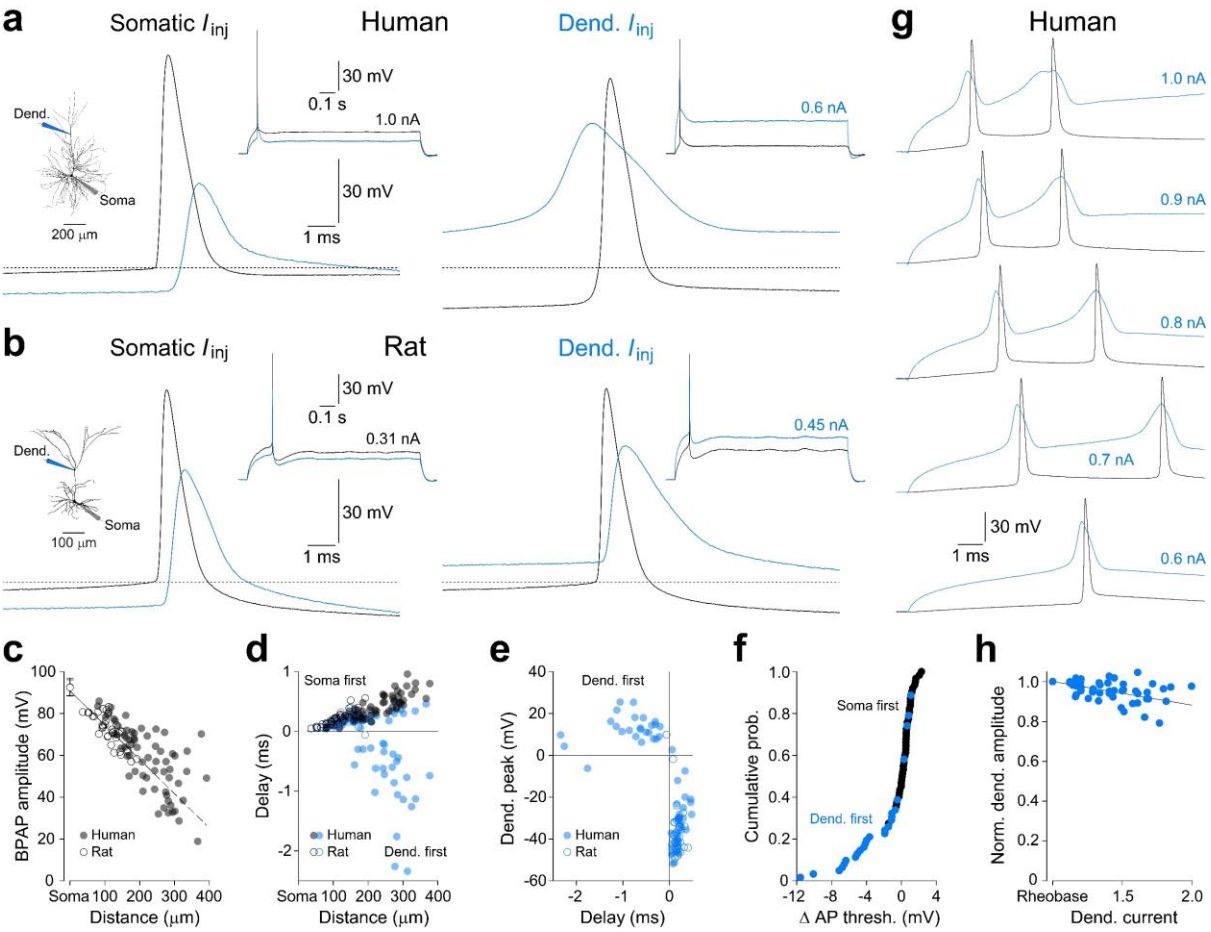

Figure 3. Dendritic excitability of human and rat L2/3 pyramidal neurons

a, Dendritic spike generation in response to the presentation of threshold dendritic positive current step (blue trace, Dend I_{inj}) in a HL2/3 pyramidal neuron. Note that the dendritic spike forward propagates to drive AP firing which has a hyperpolarized threshold (dashed line). The morphology of the recorded neuron and full evolution of voltage responses are shown inset, together with the amplitude of current steps. **b,** Threshold positive current steps delivered at somatic and dendritic sites in a RL2/3 pyramidal neuron evoke similar patterns of regenerative activity. **c,** Quantification of the distance-dependency of BPAP amplitude in rat (open symbols) and human (filled symbols) L2/3 pyramidal neurons. The average amplitude (± S.D.) of APs at the soma are shown. The continuous line represents a fit to the distance-dependent decrement of BPAPs in RL2/3 pyramidal neurons and has been extrapolated (dashed line). **d,** The delay between somatic APs and BPAPs (black symbols) generated by somatic I_{inj} and regenerative spikes evoked by dendritic I_{inj} (blue symbols). Note the distance-dependent generation of dendritic spikes which precede APs (negative times) in HL2/3 pyramidal neurons. **e,** At the time of AP initiation the voltage of dendritic spikes which

preceded AP firing (negative times) typically overshot 0 mV in HL2/3 pyramidal neurons (filled symbols). **f,** Cumulative probability distribution of the difference in the voltage threshold for AP initiation when APs were driven by somatic and dendritic I_{inj} in HL2/3 pyramidal neurons. Blue symbols represent APs driven by dendritic spikes (Dend. first). **g,** Dendritic spikes are generated across a wide suprathreshold range in HL2/3 pyramidal neurons. **h,** The peak voltage of dendritic spikes does not markedly attenuate with increasing excitatory drive. The peak voltages of dendritic spikes are shown relative to threshold values (rheobase), to allow comparison between neurons; the line represents a linear regression.

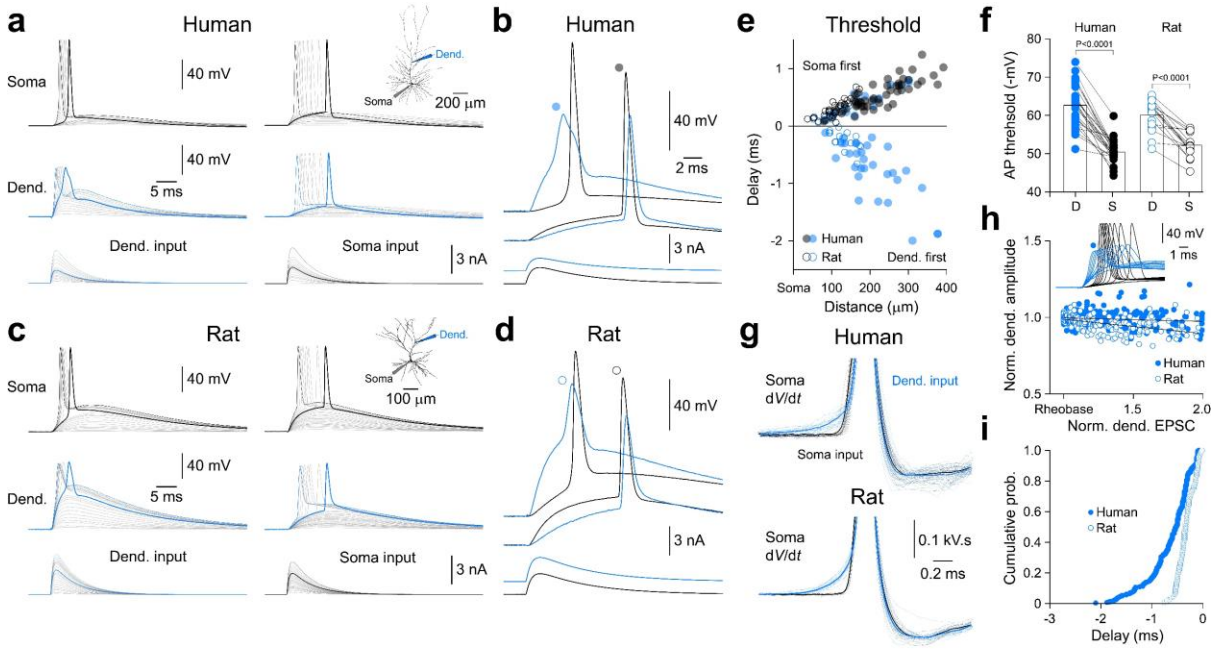

Figure 4. Stereotyped dendritic spikes are driven by physiologically relevant stimuli in human and rat layer 2/3 pyramidal neurons

a, Dendritic spikes (Dend, blue) drive AP firing in HL2/3 pyramidal neurons when generated by simulated EPSPs. Note that families of dendritic sEPSPs evoked dendritic spikes at threshold (demarked by bold traces), a pattern of activity preserved as the amplitude of the sEPSPs was further increased. In contrast, families of somatic sEPSPs evoked APs, followed by dendritic BPAPs. The morphology of the neuron and placement of recording electrodes are shown inset. **b,** Threshold firing patterns evoked by dendritic and somatic sEPSCs at a higher time-base. **c-d,** Near identical pattern of active dendritic integration of simulated synaptic input in a RL2/3 pyramidal neuron. **e,** Pooled data show that threshold somatic sEPSPs generated APs which preceded dendritic BPAPs (black symbols), in contrast, threshold sEPSPs presented at dendritic sites >100 µm from the soma typically evoked dendritic spikes which preceded APs (negative times) in HL2/3 (filled blue symbols) and RL2/3 (open blue symbols) pyramidal neurons. **f,** Significant difference in AP initiation threshold when AP firing was evoked by dendritic (D) sEPSPs which drove dendritic spikes, and somatic (S) sEPSCs (t-test, *P* values shown). **g,** First derivative (d*V*/d*t*) of somatically recorded APs evoked by dendritic (blue) and somatic input (black) in HL2/3 (27 overlain recordings) and RL2/3 (17 overlain recordings) pyramidal neurons. The bold traces represent digital averages; note the characteristic ramp preceding the AP upstroke when APs were driven by dendritic spikes (blue traces, Dend. input). **h,** Dendritic spike

amplitude does not decrement when generated across a wide suprathreshold sEPSC range in HL2/3 (filled symbols) and RL2/3 (open symbols) pyramidal neurons. Values are relative to threshold (rheobase) and have been fit by linear regression. The inset shows overlain dendritic (blue, 260 μm from soma) and somatic voltage responses evoked by sEPSP families in a human L2/3 pyramidal neuron. **i,** Cumulative probability distribution of time delay between dendritic spikes and APs for suprathreshold events generated by families of dendritic sEPSPs shown in panel h.

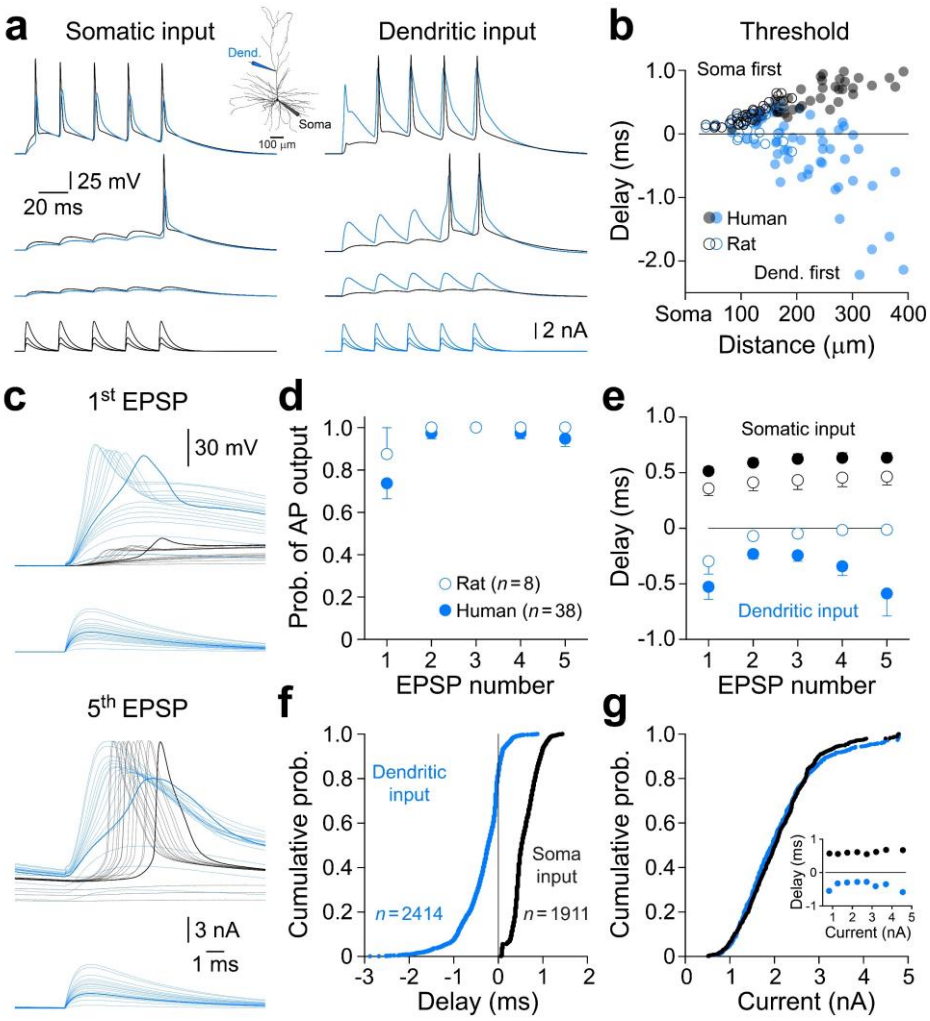

Figure 5. Dendritic spikes can be generated at high frequency in human and rat L2/3 pyramidal neurons

a, Repetitive dendritic spike generation driven by simulated EPSP trains (lower overlain traces) in HL2/3 pyramidal neurons. The morphology of the neuron and placement of recording electrodes is shown inset. **b,** Timing relationship between regenerative events generated by threshold sEPSP trains generated at the soma (black symbols) or dendrite (blue symbols). **c,** Baselined first and fifth sEPSPs of the train at a faster time base (same neuron as A). Note that the first sEPSP is crowned by the generation of dendritic spikes which drive somatic spikelets across a wide suprathreshold range, while the last sEPSP of the train is crowned by dendritic spikes which drive AP output. Threshold events are shown in bold. **d,** Pooled data describing the probability of AP firing generated in response to suprathreshold sEPSP trains in human and rat L2/3 pyramidal neurons. **e,** Pooled data showing the timing of regenerative events for each EPSP of the train. **f,** Cumulative probability distribution

of the timing of all regenerative events evoked by dendritic (blue) and somatic (black) sEPSP trains in HL2/3 pyramidal neurons. Note the clear disparity between the timing relationship and the preponderance of APs driven by dendritic spikes (negative times) when sEPSP trains were presented at dendritic sites. **g,** Cumulative probability distributions of amplitude of the current underlying sEPSPs (dendritic, blue), which drove the regenerative events shown in (f). The inset shows the average time delay between the regenerative events evoked by somatic and dendritic EPSPs at the indicated binned amplitudes of the driving current.

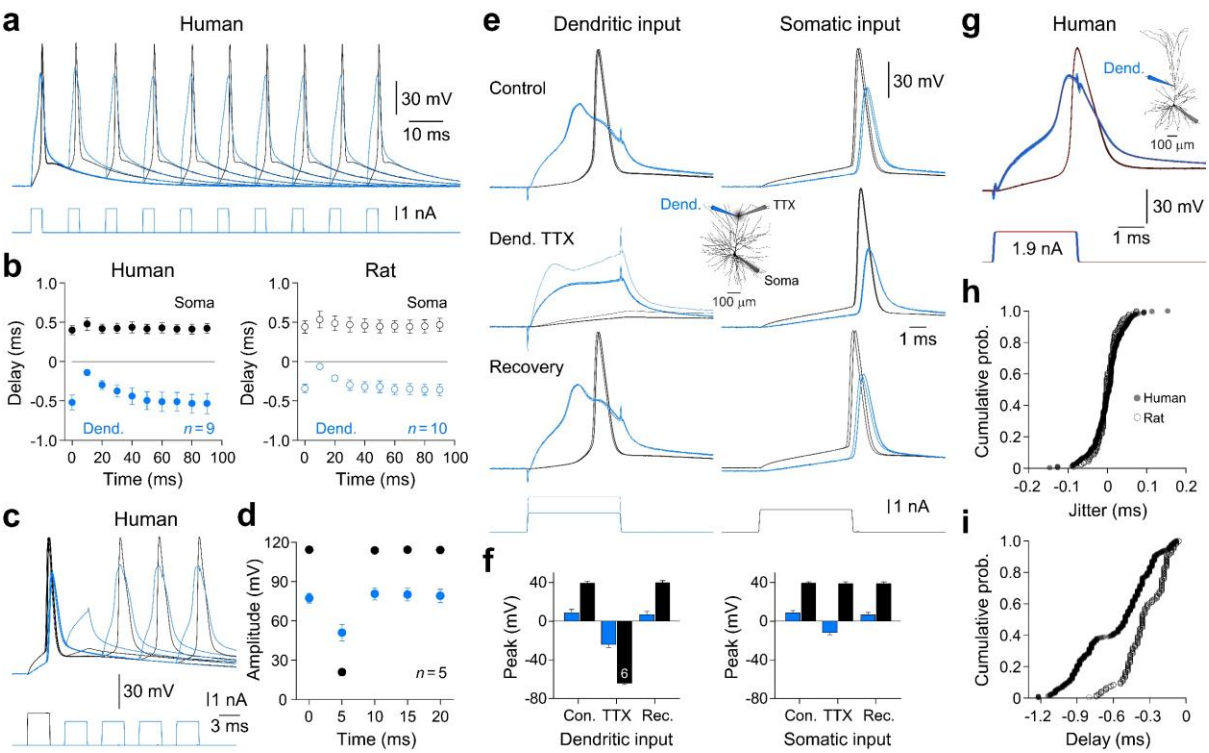

Fig. 6. High-fidelity dendritic spikes are mediated by dendritic sodium channels in human L2/3 pyramidal neurons

a, Initiation of dendritic spikes at high repetition frequencies in HL2/3 pyramidal neurons. Each dendritic spike was generated in response to a short positive current step, separated in time by Δ10 ms. **b,** Quantification showing that dendritic spike generation leads AP firing (negative times) in human and RL2/3 pyramidal neurons when generated by dendritic current steps (Dend.) at the indicated intervals. **c,** AP initiation transiently precludes dendritic spike generation. In each overlain trial, AP firing was driven by the presentation of a threshold somatic current step (black, lower trace), which was followed in time by the presentation of threshold dendritic current steps at Δ5 ms intervals; note that at the first interval dendritic spike initiation did not occur. **d,** Pooled data of the peak amplitude of somatic (black) and dendritic (blue) voltage responses showing the transient suppression of dendritic spike generation by AP firing. **e,** Dendritic spikes are mediated by sodium channels in HL2/3 pyramidal neurons. Overlain voltage traces show dendritic (blue) and somatic (black) voltage responses evoked by brief dendritic or somatic positive current steps (lower traces). The transient local dendritic application of TTX (2 μM) blocked the initiation of dendritic spikes but did not alter the characteristics of APs generated by somatic positive current pulses. A partial reconstruction of the morphology of the HL2/3 pyramidal neuron is

shown inset, illustrating the recording and TTX application sites. **f,** Pooled data describing the blockade of dendritic spikes and the reduction of the amplitude of BPAPs by the local dendritic application of TTX. Bars resent mean ± S.E.M.. **g,** Overlain voltage traces (30 trials) aligned at the peak of somatic APs show the minimal trial-to-trial variation in dendritic spike to AP coupling around digital averages (red traces). The morphology of the HL2/3 pyramidal neuron is shown inset. **h,** Trial-to-trial temporal jitter around the mean dendritic spike to AP time-delay for HL2/3 (filled symbols, n= 12) and RL2/3 (open symbols, n= 11) pyramidal neurons. **i,** Cumulative probability distribution of the time-delay between dendritic spikes and APs for the data shown in panel h.

Supplementary Information

High-fidelity dendritic sodium spike generation in human layer 2/3 neocortical pyramidal neurons

Helen M. Gooch[1,2], Tobias Bluett[1], Madhusoothanan B. Perumal[1], Hong D. Vo[1], Lee N. Fletcher[1], Jason Papacostas[2], Rosalind L. Jeffree[3], Martin Wood[2], Michael J. Colditz[3], Jason McMillen[2], Tony Tsahtsarlis[2], Damian Amato[2], Robert Campbell[2], Lisa Gillinder[1,2], and Stephen R. Williams[1,2,*]

Supplementary Figs. 1-8

Supplementary Tables 1-2

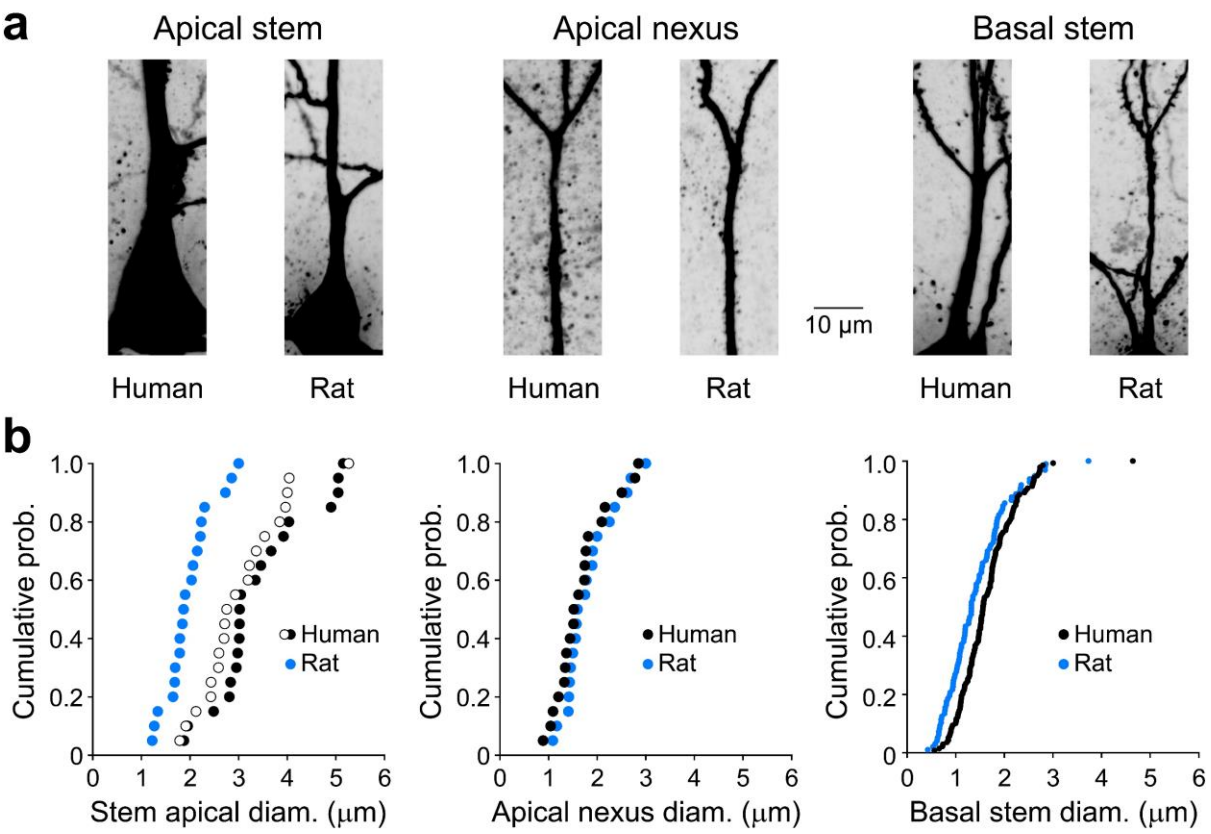

Supplementary Fig. 1. Diameter of human and rat L2/3 pyramidal neuron dendrites

a, Representative confocal images of dendritic segments in human and rat layer 2/3 pyramidal neurons. Images from the indicated sites were taken from the neurons, selected to be representative of average diameters. **b,** Pooled analysis of the diameter of apical and basal dendrites of human and rat layer 2/3 pyramidal neurons. The diameters of stem apical and basal dendrites were significantly different (apical stem: human= 3.43 ± 0.22 µm, rat= 1.98 ± 0.11 µm, Mann Whitney U= 28, *P*< 0.0001; basal stem: human= 1.66 ± 0.05 µm, rat= 1.44 ± 0.06 µm, Mann Whitney U= 5142, *P*= 0.0019). The open black symbols represent measurement of the diameter of stem apical dendrites in HL2/3 neurons over the distal 10 µm of the segment (apical stem: human (distal 10 µm) = 3.07 ± 0.19 µm, rat= 1.98 ± 0.11 µm, t-test, df= 38, *P*< 0.0001). Note, however, that the diameters of apical dendritic segments measured over a segment 20 µm proximal to the first main bifurcation of the apical dendritic tree (nexus) are similar between human and rat L2/3 pyramidal neurons (apical nexus: human= 1.69 ± 0.12 µm, nexus= 309 ± 54 µm from soma; rat= 1.82 ± 0.12 µm, nexus= 155 ± 20 µm from soma; t-test, df= 38, *P*= 0.4425).

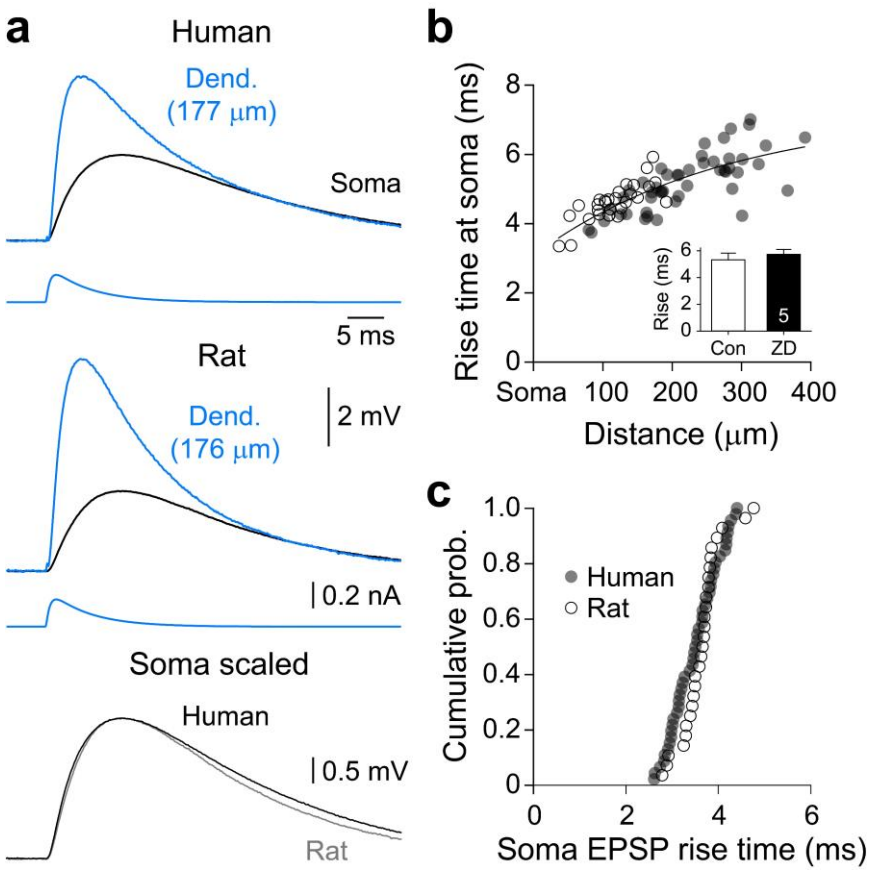

Supplementary Fig. 2. Somatic rise time of dendritic simulated EPSPs

a, Simulated dendritic EPSPs generate somatic voltage responses with similar rise times in human and rat L2/3 pyramidal neurons. Simultaneous recordings of somatic (black traces) and apical dendritic (blue traces) voltage are shown together with the driving current (lower traces). The lower overlain traces (soma scaled) show that the somatic rise-time of EPSPs generated at similar dendritic locations are nearly identical in a human and rat L2/3 pyramidal neuron. **b**, Quantification of the distance-dependent increase in the 10-90 % rise time of somatic sEPSPs generated at the indicated apical dendritic sites in HL2/3 (filled symbols) and RL2/3 (open symbols) pyramidal neurons. Data have been fit by an exponential function with a length constant of 279 μm. The inset shows that blocking HCN channels with ZD7288 (10 μM) in HL2/3 pyramidal neurons has little impact on the somatic rise time of dendritically generated sEPSPs. Bars represent mean ± S.E.M.. **c,** Cumulative probability distributions demonstrate the similar 10-90 % rise times of somatically generated and recorded sEPSPs in HL2/3 (filled symbols) and RL2/3 (open symbols) pyramidal neurons.

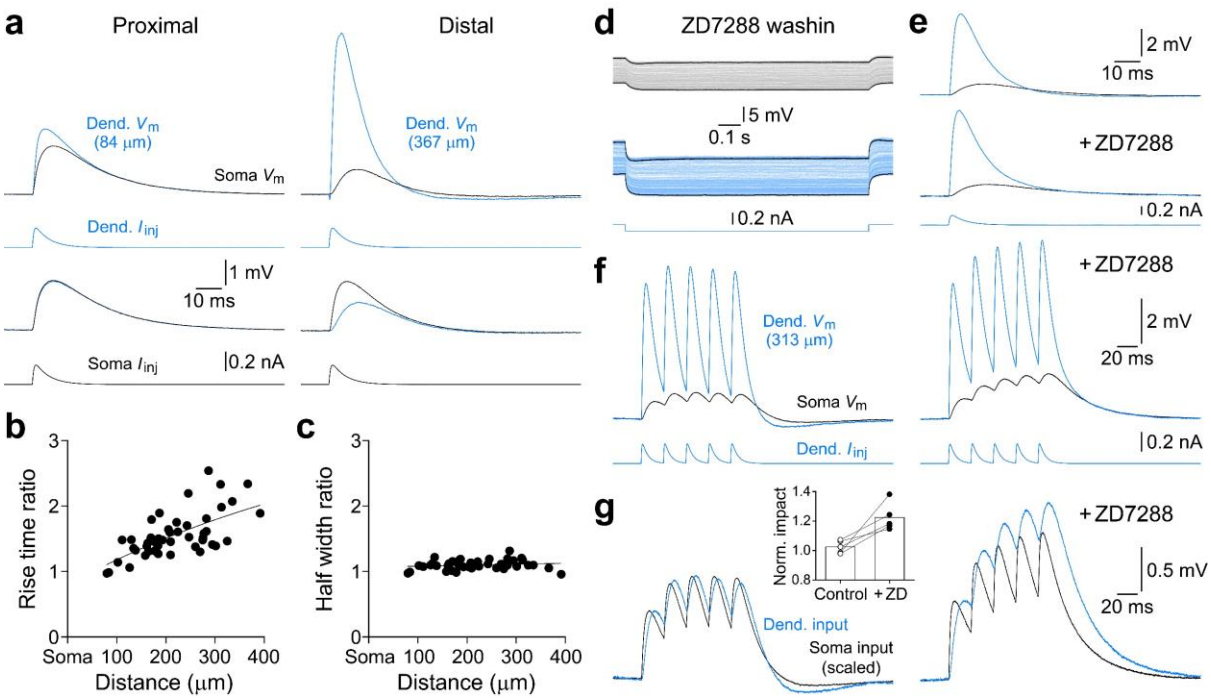

Supplementary Fig. 3. HCN channels sculpt dendritic sEPSPs in human L2/3 pyramidal neurons

a, Representative simultaneous somatic (black traces) and dendritic (blue traces) recordings of sEPSPs showing the distance-dependent pattern of dendro-somatic and somato-dendritic voltage attenuation. **b-c,** Quantification of the dendritic distance-dependent increase of the somatic rise time of sEPSPs, but the distance-dependent preservation of the somatic half-width of dendritically generated sEPSPs. Values represent the ratio of the kinetics of somatically recorded sEPSPs when generated at the soma and from the indicated dendritic sites in each tested HL2/3 pyramidal neuron. Data in panel b were fit with an exponential function with a length constant of 637 μm (line). Data in panel c were fit by linear regression, with a slope of 0.148 per mm (line). **d,** HCN channels powerfully control the resting membrane potential of HL2/3 pyramidal neurons. Simultaneous recording of somatic (grey traces) and dendritic (blue traces, 369 μm) voltage responses generated by a negative dendritic current step (lower trace) under control and during the application of ZD7288 (10 μM). The overlain black traces represent digital averages compiled under control conditions and in the presence of ZD7288. Pooled results demonstrated that the application of ZD7288 significantly hyperpolarized the resting membrane potential of HL2/3 neurons (control soma= -72.6 ± 0.8 mV, ZD soma= -80.5 ± 1.8 mV, n= 5; paired t-test, P= 0.0052; control dendrite= -70.0 ± 1.5 mV, ZD dendrite= -77.7 ± 2.7 mV; paired t-test, P< 0.0151; average distance from the soma: 255 ± 39 μm). **e,** The pharmacological blockade of HCN channels eliminated the cross-over in the decay phase of dendritic (blue traces) and somatic (black traces) voltage responses generated by a dendritic simulated excitatory postsynaptic current waveform delivered 312 μm from the soma (lower trace). **f,** Temporal summation of sEPSP trains simultaneously recorded at the dendritic site of generation (blue traces) and the soma (black traces). Note the greater temporal summation of sEPSP trains when HCN channels were blocked with ZD7288

(10 μM). **g,** The somatic impact of dendritic sEPSP trains is controlled by HCN channels. The amplitude of the first somatically recorded sEPSP of the train has been peak scaled, same neuron as in panels e and f. The inset shows quantification of the enhanced summation of dendritically generated sEPSPs in ZD7288.

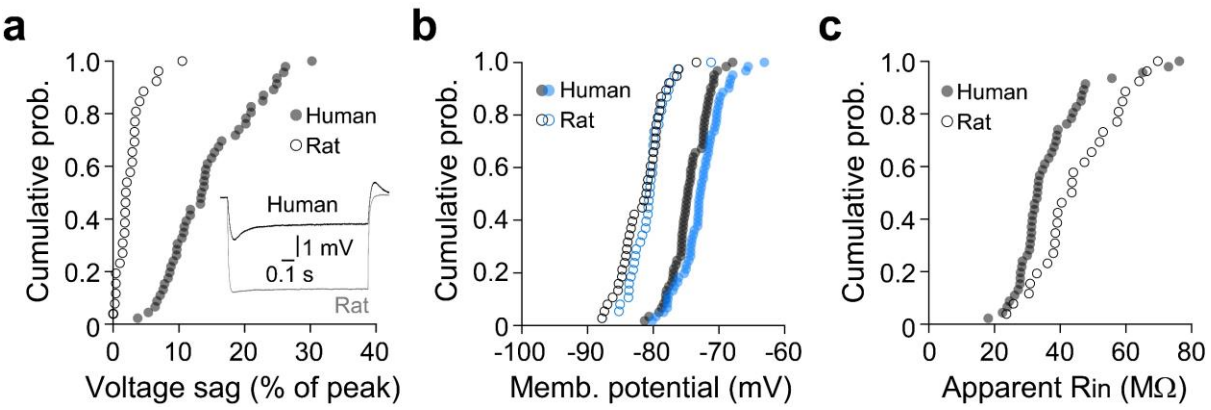

Supplementary Fig. 4. Electrophysiological properties of human and rat L2/3 pyramidal neurons

a, Somatic voltage sag (% of peak) apparent during negative voltage responses (inset) is greater in HL2/3 pyramidal neurons (Mann Whitney U= 23, *P*< 0.0001). **b,** Distribution of somatic (black) and apical dendritic (blue) membrane potential of human (filled symbols) and rat L2/3 (open symbols) pyramidal neurons, distributions are significantly different between species (soma: t-test, df= 97, *P*< 0.0001; dendrite: *P*< 0.0001). **c,** The peak somatic apparent input resistance of human and rat L2/3 pyramidal neurons is distinct (Mann Whitney U= 344, *P*< 0.0026).

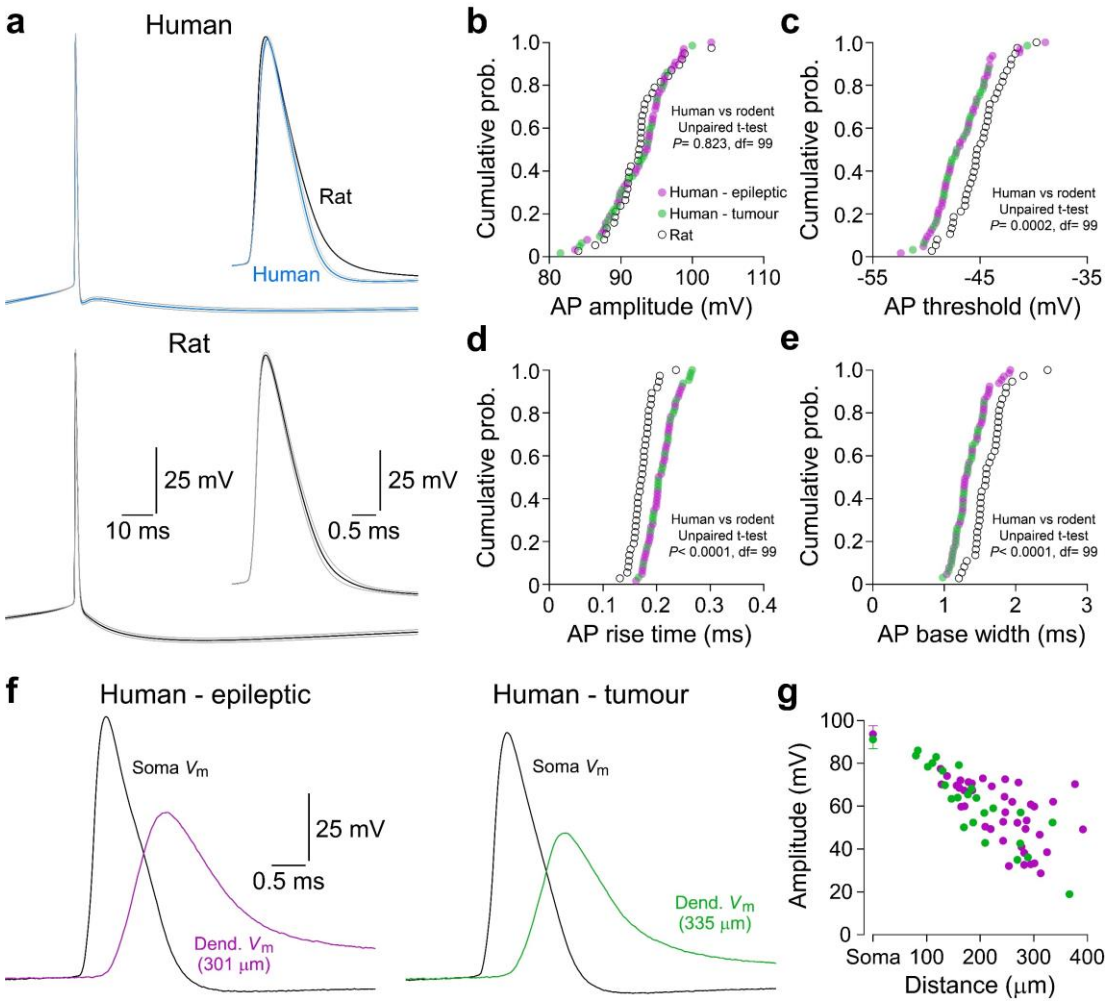

Supplementary Fig. 5. Properties of APs and BPAPs in human and rat L2/3 pyramidal neurons

a, Averaged waveform of somatically recorded APs from 51 HL2/3 (blue) and 35 rat (black) L2/3 pyramidal neurons. APs were generated by the presentation of somatic rheobase positive current steps. The grey lines represent error around the mean (± 2 S.E.M.). Note the characteristic differences in AP after-hyperpolarizing potentials. The averaged APs are shown inset at a faster time-base to illustrate the rise- and decay time course. **b-e,** Cumulative probability distributions of the indicated properties of APs recorded from human and rat L2/3 pyramidal neurons. Human neurons are delineated by etiology. Note that the properties of APs recorded from patients who underwent surgery for the removal of sub-cortical brain tumours (green symbols) or the alleviation of refractory epilepsy (magenta symbols) intermingle throughout the distributions. For each panel the results of statistical comparison between human and rat L2/3 pyramidal neurons are shown. **f,** Representative waveforms of somatic APs and simultaneously recorded dendritic BPAPs in HL2/3 pyramidal neurons recorded from patients who had undergone surgery for the removal of a sub-cortical brain tumour and the alleviation of refractory epilepsy. **g,** Distance-dependency of the amplitude of BPAPs in HL2/3 pyramidal neurons delineated by patient etiology. The average amplitude of somatically recorded APs (± S.D.) is shown.

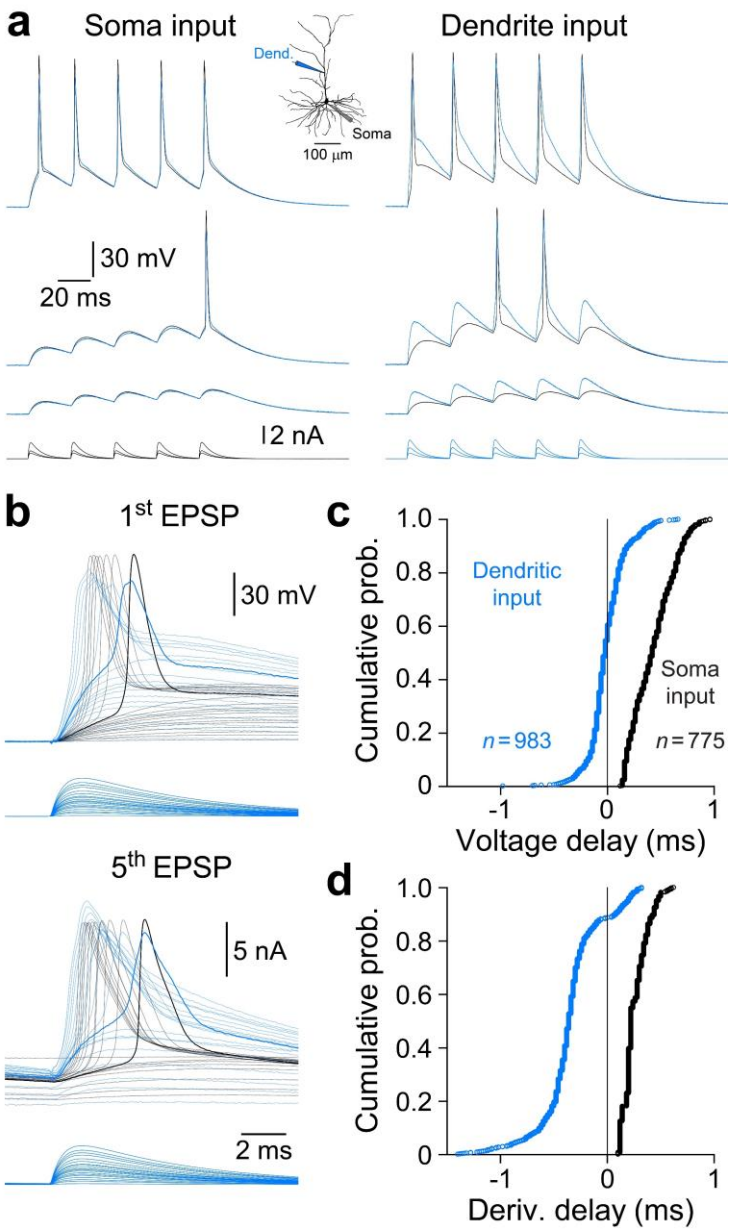

Supplementary Fig. 6. Dendritic spikes are generated at high frequencies in rat L2/3 pyramidal neurons

a, Repetitive dendritic spike generation is driven by simulated excitatory postsynaptic current trains (lower overlain traces) in a RL2/3 pyramidal neuron. The morphology of the neuron and placement of recording electrodes is shown inset. **b,** Baselined sEPSPs generated by the first and fifth sEPSP of the train at a faster time base (same neuron as a). Note that dendritic spikes drive AP firing over a wide suprathreshold range. **c-d,** Cumulative probability distributions of the timing of all regenerative events evoked by dendritic (blue) and somatic (black) sEPSP trains in RL2/3 pyramidal neurons. The time difference was calculated at peak voltage of events in c, and by the time difference between the peak amplitude of the first derivative of events in d. Note the clear disparity between timing relationship, and the preponderance of APs driven by dendritic spikes (negative times) when sEPSP trains were presented at dendritic sites.

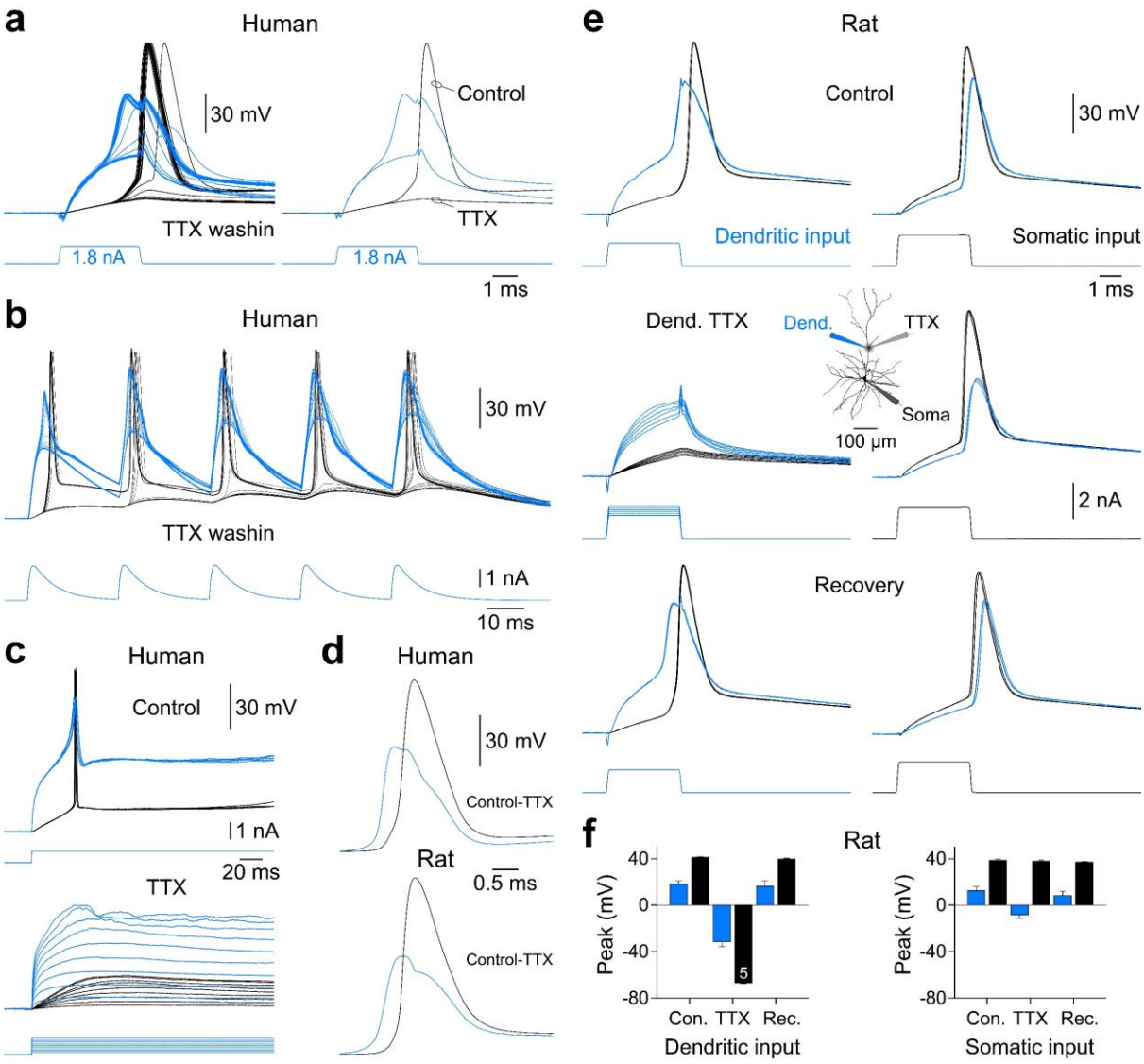

Supplementary Fig. 7. Dendritic sodium spikes in rat and human L2/3 pyramidal neurons

a, The bath application of TTX (1 μM) blocks regenerative dendritic spikes evoked by a threshold short dendritic positive current pulse in a HL2/3 pyramidal neuron. Note the blockade of dendritic spikes and APs as TTX is washed into the bath. The traces on the right side show the waveform of a dendritic spike and coupled AP under control and the electrotonic responses generated in the presence of TTX. **b,** Dendritic spikes generated repetitively by a train of simulated dendritic excitatory postsynaptic currents are blocked by the bath application of TTX in a HL2/3 pyramidal neuron. Note the abolition of dendritic spikes and APs as TTX is washed into the bath. **c,** Overlain traces of dendritic spikes generated in response to threshold long dendritic current steps (upper traces) are blocked by the bath application of TTX (1 μM, lower overlain traces). In the presence of TTX regenerative activity is abolished across a wide positive voltage range. **d,** Representative waveforms of TTX subtracted dendritic spikes and APs evoked by threshold positive current steps in a human and rat L2/3 pyramidal neuron. **e,** Overlain voltage traces show dendritic (blue) and somatic (black) responses evoked by brief dendritic or somatic positive current steps (lower traces) in a RL2/3 pyramidal

neuron. The transient local dendritic application of TTX (2 μM) blocked the initiation of dendritic spikes but did not alter the characteristics of APs generated by somatic positive current pulses. A reconstruction of the morphology of the RL2/3 pyramidal neuron is shown inset, illustrating recording and TTX application sites. **(F)** Pooled data describing the blockade of dendritic spikes and the reduction of the amplitude of BPAPs by the local dendritic application of TTX. Bars represent mean ± S.E.M..

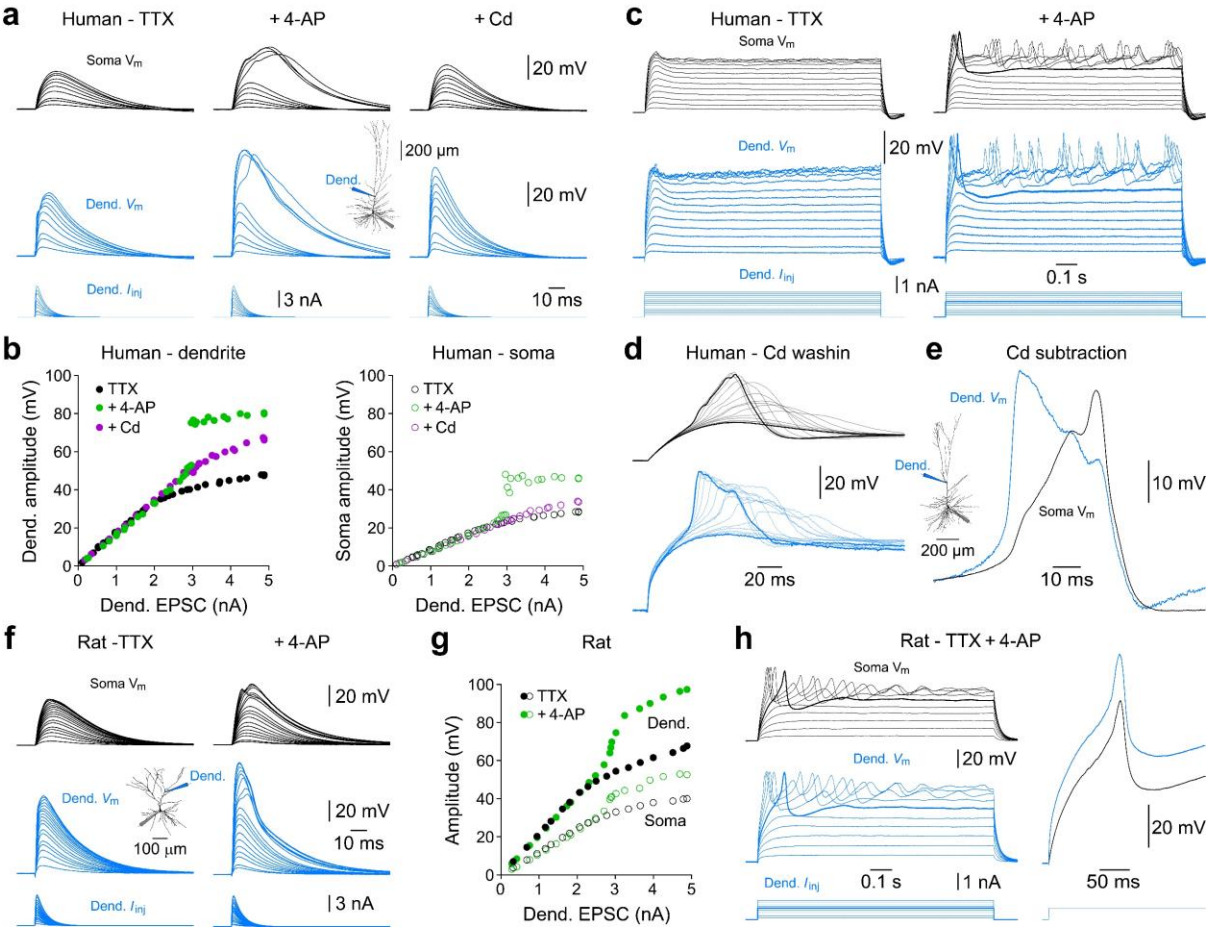

Supplementary Fig. 8. Pharmacological blockade of potassium channels unmasks dendritic calcium electrogenesis in human and rat L2/3 pyramidal neurons

a, Simultaneous somatic and apical dendritic recording of families of simulated dendritic EPSPs recorded under the indicated conditions from a HL2/3 pyramidal neuron (morphology and recording sites inset). Note, the absence of dendritic regenerative activity when sodium channels were blocked with tetrodotoxin (TTX, 1 µM), but the generation of powerful dendritic electrogenesis following the addition of the voltage-gated potassium channel antagonist 4-amino pyridine (4-AP, 5 mM). Under these conditions dendritic regenerative activity was blocked by the addition of the broad-spectrum voltage-gated calcium channel antagonist cadmium (Cd, 100 µM). **b**, Measurement of the peak amplitudes of dendritic sEPSPs at dendritic site of generation (left graph) and the soma (right graph) under the indicated conditions, same HL2/3 pyramidal neuron as panel a. **c**, Families of voltage responses evoked by the injection of long steps of positive current at the dendritic recording site (160 µm from the soma) of a HL2/3 pyramidal neuron under the indicated conditions. Note the absence of dendritic regenerative activity in the presence of TTX (1 µM), but the unmasking of repetitive regenerative dendritic activity by the bath addition of 4-AP (5 mM). The threshold response is demarked by bold traces. **d**, The bath application of cadmium (100 µM) blocks dendritic electrogenesis recorded in the presence of TTX (1 µM) and 4-AP (5 mM) from a HL2/3 pyramidal neuron (morphology and recording sites inset). The bold traces delineate control (TTX and 4-AP) and cadmium

conditions. **e**, The waveform of cadmium subtracted dendritic calcium electrogenesis recorded at dendritic site of generation and the soma, same HL2/3 pyramidal neuron as shown in panel d. **f**, Simultaneous somatic and apical dendritic recording of families of simulated dendritic EPSPs recorded under the indicated conditions from a RL2/3 pyramidal neuron (morphology and recording sites inset). Note, the absence of dendritic regenerative activity when sodium channels were blocked with tetrodotoxin (TTX, 1 μM), but the generation of dendritic electrogenesis following the blockade of voltage-gated potassium channels with 4-amino pyridine (4-AP, 5 mM). **g**, Measurement of the peak amplitudes of sEPSPs at dendritic site of generation (filled symbols) and the soma (open symbols) under the indicated conditions. **h**, Families of voltage responses evoked by the injection of long steps of positive current at the dendritic recording site of the same RL2/3 pyramidal neuron in the presence of TTX (1 μM) and 4-AP (5 mM). Note the generation of robust calcium electrogenesis. The threshold response if delineated by the bold traces and shown at a faster time-base inset.

Supplementary Table 1. Information on patients with refractory epilepsy

#	Age	Sex	Diagnosis	Age of epilepsy onset	Recent antiepileptic drugs	Anaesthetic	Paralytic agent	Resected brain region
1	55	M	Epilepsy - hippocampal sclerosis	20	LTG, BRV, CBZ, CLB	PRO, REM, SEV, FEN	ROC	L-temporal
2	25	F	Epilepsy - mesial temporal sclerosis	5	TOP, LTG, LCM	PRO, REM	ROC	L-temporal
3	22	M	Epilepsy	15	OXC, BRV, LCM, ZNS, CLB	PRO, REM, FEN, MID	ROC	L- temporal
4	32	M	Epilepsy - focal cortical dysplasia	childhood	LEV, LCM, LTG	PRO, REM, FEN	VEC	R-temporal
5	42	M	Epilepsy - mesial temporal sclerosis	24	PER, CBZ, LCM, BRV	PRO, REM	ROC	R-temporal
6	17	M	Epilepsy - Dysembryoplastic neuroepithelial tumor (DNET)	15	PER, OXC, BRV, LTG, CLB	PRO, REM, FEN	VEC	L-temporal
7	54	M	Epilepsy - mesial temporal sclerosis	39	LCM, LEV	PRO, REM	ROC	L-temporal
8	23	M	Epilepsy - hippocampal sclerosis	13	CLB, CBZ	PRO, REM	ROC	R-temporal
9	22	F	Epilepsy - focal cortical dysplasia-like	5	ZNS, BRV, LCM	PRO, REM, FEN	VEC	L-temporal

Abbreviations

Antiepileptic agents: LEV – levetiracetam, LTG – lamotrigine, CBZ – carbamazepine, LCM – lacosamide, OXC – oxcarbazepine, CLB – clobazam, ZNS – zonisamide, BRV – brivaracetam, PER – perampanel, TOP – topiramate.

General anaesthesia maintenance: PRO – propofol, REM – remifentanil, SEV – sevoflurane, FEN – fentanyl, MID – midazolam, LIG – lignocaine.

Paralytic agents: ROC – rocuronium, VEC – vecuronium.

L – left, R – right.

Supplementary Table 2. Information on patients with subcortical tumours

#	Age	Sex	Diagnosis	Recent antiepileptic drugs	Anaesthetics	Paralytic agent	Resected brain region	5-ALA
1	70	F	Tumour - glioblastoma	LEV (during surgery)	PRO, REM, FEN, MID	VEC	L-temporal	No
2	50	F	Tumour - glioblastoma	LEV	PRO, REM	ROC	R-temporal	Yes
3	69	F	Tumour - glioblastoma	LEV	PRO, REM	ROC	L-temporal	Yes
4	37	M	Focal cortical dysplasia	LTG, LEV, PER	PRO, REM, LIG	ROC	L-temporal	No
5	59	M	Tumour - glioma	N/A	PRO, REM, FEN, MID	VEC	R-temporal	No
6	60	F	Tumour - meningioma	N/A	PRO, REM, LIG	VEC	R-temporal	No

Abbreviations

Antiepileptic agents: LEV – levetiracetam, LTG – lamotrigine, PER – perampanel.

General anaesthesia maintenance: PRO – propofol, REM – remifentanil, FEN – fentanyl, MID – midazolam, LIG – lignocaine.

Paralytic agents: ROC – rocuronium, VEC – vecuronium.

Imaging agent: 5-ALA – 5-aminolevulinic acid.

L – left, R – right.